

Banner appropriate to article type will appear here in typeset article

# On the analytical behavior of the $k-\omega$ turbulence model in buoyant-driven thermal convection

**Da-Sol Joo**

Department of Mechanical Engineering, Pohang University of Science and Technology, Pohang, Gyeongbuk 37673, South Korea

**Corresponding author:** D.-S. Joo, [wnekthf3818@postech.ac.kr](mailto:wnekthf3818@postech.ac.kr)

(Received xx; revised xx; accepted xx)

---

The representation of buoyancy-driven turbulence in Reynolds-averaged Navier–Stokes models remains unresolved, with no widely accepted standard formulation. A key difficulty is the lack of analytical guidance for incorporating buoyant effects, including the treatment of the scale-determining equations under unstable stratification. This study derives an analytical solution of the standard  $k-\omega$  model for Rayleigh–Bénard convection in a horizontally infinite plane layer, where turbulent kinetic energy is generated solely by buoyancy. The solution provides explicit scaling relations among the Rayleigh ( $Ra$ ), Prandtl ( $Pr$ ), and Nusselt ( $Nu$ ) numbers that capture the trends observed in numerical simulations:  $Nu \sim Ra^{1/3} Pr^{1/3}$  for  $Pr \ll 1$  and  $Nu \sim Ra^{1/3} Pr^{-0.415}$  for  $Pr \gg 1$ . Although this analytical framework provides a consistent reference for understanding how buoyancy enters the  $k-\omega$  closure, the predicted  $Nu$  scaling differs from experimental measurements. The buoyancy-related modelling terms are therefore reformulated to reproduce observed heat-transport trends across wide  $Ra$  and  $Pr$  ranges. By introducing only two additional dimensionless algebraic functions and recovering the original formulation when buoyancy is absent, the resulting corrections retain full compatibility with the standard  $k-\omega$  framework. The revised closures are validated across a range of configurations, including one- and two-dimensional Rayleigh–Bénard convection, internally heated convection, unstably stratified Couette flow, and vertically heated natural convection with varying aspect ratios. Across all cases, the corrected formulation yields substantially improved quantitative accuracy.

**Key words:**

---

## 1. Introduction

Buoyancy-driven turbulence is common in nature, spanning the oceans and atmosphere, and central to engineering, including indoor ventilation and nuclear safety. For such flows, Reynolds-averaged Navier–Stokes (RANS) closures remain widely used in engineering applications owing to their favourable accuracy-to-cost ratio, with two-equation models such as the standard  $k-\varepsilon$  and  $k-\omega$  formulations being particularly common.

Recent references and review works on buoyancy-related RANS modelling can be found in Hanjalić (2002); Burchard (2007); Launder (2005); Durbin & Pettersson-Reif (2011); Hanjalić & Launder (2011); Durbin (2018); Hanjalić & Launder (2021). In natural convection, temperature acts as an active scalar that modifies the momentum field through buoyancy. The exact transport equation for turbulent kinetic energy ( $k$ ) contains an explicit buoyancy-production term proportional to the inner product between the turbulent heat flux and gravity; the term is negative in stable stratification and positive in unstable stratification. Because the modelled  $k$  equation in both  $k$ - $\varepsilon$  and  $k$ - $\omega$  frameworks is derived from this exact equation, it is standard to include buoyant production in  $k$ .

The central controversy concerns the scale-determining equation—namely, the dissipation ( $\varepsilon$ ) or dissipation-per-unit- $k$  ( $\omega$ ) equation—which is usually the sole source of buoyancy-related modelling terms in two-equation RANS closures. As summarised in reference works (Burchard 2007; Hanjalić & Launder 2011) and articles (Henkes *et al.* 1991; Peng & Davidson 1999; Hanjalić & Vasić 1993; Hanjalić & Launder 2021), there is no universally accepted prescription for representing buoyancy at this level. Broadly, two lines of work can be distinguished. One omits any buoyant contribution from the scale-determining equation. The rationale is that shear production there can be motivated by canonical shear-flow analyses, whereas an analogous justification for a buoyant counterpart in  $\varepsilon$  or  $\omega$  is lacking (Markatos & Pericleous 1984). The other line of work adds a buoyancy term to the scale-determining equation, modelling it by analogy with shear production and using the same functional form as the shear-production term in the  $\varepsilon$ - or  $\omega$ -equation. As described by Hanjalić & Vasić (1993), in flows such as Rayleigh–Bénard convection, where shear production is nearly zero but buoyant production dominates, omitting the buoyant-production term from the  $\varepsilon$  equation can render  $\varepsilon$  a pure sink; when combined with finite buoyant production in  $k$ , this may lead to unphysical growth of  $k$ . A number of empirical blends have also been proposed for specific regimes (Rodi 1980, 1987; Henkes *et al.* 1991; Hanjalić & Vasić 1993; Peng & Davidson 1999). A frequently cited guideline is to suppress buoyant contributions under stable stratification while adding them under unstable stratification, using the same functional form as the shear-production term (Rodi 1987). Each of these studies explicitly acknowledged the empirical nature of their proposed treatments, and the proper representation of buoyancy in two-equation RANS closures remains an open issue.

The lack of a unified criterion arises from the absence of theoretical analyses that establish how standard two-equation closures behave in canonical, buoyancy-dominated flows. In contrast, in shear-driven canonical flows, the analytical behaviour of standard RANS models is well established: they reproduce classical results—the logarithmic velocity law with the von Kármán constant, boundary-layer scaling, spreading rates of free-shear flows, and self-similarity in homogeneous shear and decaying turbulence. Such benchmarks have served both to justify the formulation of the models and to calibrate their coefficients (Pope 2000; Wilcox 2006).

Specifically, to the author's knowledge, analytical criteria are available for modelling stably stratified flows, whereas corresponding criteria for unstable stratification remain scarce. In the stable regime, linear-stability analyses of stably stratified shear flows provide a clear physical measure of flow suppression, commonly formulated in terms of the flux Richardson number. This quantity, defined locally as the ratio of buoyant to shear production, attains a critical value of  $Ri_f = 0.25$ , beyond which stratification begins to stabilise the shear flow. Owing to this well-established threshold,  $Ri_f$  has long served as a practical modelling reference (Gibson & Launder 1978; Durbin & Pettersson-Reif 2011), guiding the selection of model constants in  $k$ - $\varepsilon$  closures (Burchard & Baumert 1995) and informing explicit algebraic closures for stable stratification (Lazeroms *et al.* 2013).

By contrast, in unstably stratified buoyant flows, an appropriate model should account for the rate at which potential energy associated with density variations is converted into the kinetic energy of thermal plumes—a mechanism fundamentally different from shear production. In homogeneous shear flow, the dynamics are primarily governed by the shear rate  $S$ ,  $k$ , and  $\varepsilon$ , yielding the local similarity relation  $\varepsilon/k \sim S$ , which is widely accepted as a standard modelling benchmark (Pope 2000; Wilcox 2006). For buoyant effects, however, evidence for such purely local self-similarity is scarce. This scarcity is often cited as an indirect justification for omitting a buoyancy term from the scale-determining equation, as in Markatos & Pericleous (1984). Instead, similarity in buoyant flows is typically expressed through global power-law relations among the Nusselt ( $Nu$ ), Rayleigh ( $Ra$ ), and Prandtl ( $Pr$ ) numbers—for example, the relation  $Nu \sim Ra^{0.31}$  reported over  $10^6 \lesssim Ra \lesssim 10^{17}$  (Niemela *et al.* 2000). Because these relations depend on global temperature differences and a domain-scale length, the assessment of buoyancy effects in two-equation closures is more appropriately undertaken through domain-integrated analyses than through purely local arguments.

Against this background, the present study adopts one-dimensional Rayleigh–Bénard convection as a canonical test bed for analysing buoyancy effects in the Wilcox (2006)  $k$ – $\omega$  model. In this configuration, the mean flow vanishes and the turbulent kinetic energy budget is governed solely by buoyant production, thereby isolating the role of the buoyancy term in the  $\omega$  equation. This case corresponds to Rayleigh–Bénard convection in a horizontally periodic plane layer, for which direct numerical simulation (DNS) budgets clearly show buoyant production dominating the  $k$  balance (Togni *et al.* 2015).

The choice of the  $k$ – $\omega$  model is motivated by its near-wall formulation with a prescribed  $\omega$  distribution, which makes analytical treatment more tractable than in the  $k$ – $\varepsilon$  model. In earlier work with a similar motivation (Joo & You 2024; Joo 2025), the role of the buoyancy term in the  $\varepsilon$  equation is examined within the  $k$ – $\varepsilon$  framework. However, in the standard  $k$ – $\varepsilon$  model, the boundary conditions of the  $\varepsilon$  equation depend on the spatial gradients of  $k$  and  $\varepsilon$ , and as a result a unique steady-state solution is not strictly assured; in a closed Rayleigh–Bénard convection configuration, the predicted  $k$  and  $\varepsilon$  can exhibit exponential growth over time depending on the initial conditions (Joo & You 2024; Joo 2025).

This difficulty does not arise in the  $k$ – $\omega$  formulation: in the  $k$ – $\omega$  model,  $\omega$  attains a peak at the wall and its near-wall distribution is prescribed solely by viscosity. Consequently, even in a Rayleigh–Bénard convection configuration, the steady-state  $\omega$  distribution is uniquely determined, thereby enabling an explicit analytical solution. Establishing such an analytical solution for the  $k$ – $\omega$  model is therefore one of the central objectives of the present study. Owing to the distinct mathematical structures of the two models, the analytical approach introduced here for the  $k$ – $\omega$  model is almost entirely independent of the prior analysis for the  $k$ – $\varepsilon$  model.

The main contributions of this study are threefold: (i) an analytical framework that clarifies how the scale-determining equation governs buoyancy-dominated turbulence and its simulation behaviour; (ii) a closed-form analytical solution for one-dimensional Rayleigh–Bénard convection under the standard  $k$ – $\omega$  closure, yielding explicit  $Nu$ – $Ra$ – $Pr$  scalings; and (iii) corrections to the buoyancy-related model terms, intended to bring the RANS closure into closer agreement with established experimental trends across broad  $Ra$  and  $Pr$  ranges.

The remainder of the paper is organised as follows. §2 presents the  $k$ – $\omega$  model of Wilcox (2006) and summarises previous treatments of buoyancy in two-equation closures. §3 derives an analytical solution for one-dimensional Rayleigh–Bénard convection, yielding an explicit relation for  $Nu$  as a function of  $Ra$  and  $Pr$ . §4 proposes a new buoyancy-correction methodology based on the established analytical solution. The buoyancy

term in the scale equation is modified, and a buoyancy-wall model is introduced into the turbulent thermal diffusivity. The resulting corrected  $\omega$  equation is formulated by synthesising the established analytical criterion for negative buoyant production with the new analytical criterion derived here for positive buoyant production. §5 further validates the proposed model beyond the one-dimensional Rayleigh–Bénard convection test case, through numerical simulations of two types of internally heated convection, unstably stratified Couette flow, Rayleigh–Bénard convection in a two-dimensional enclosure, and vertically heated natural convection with varying aspect ratios. Finally, §6 concludes the paper.

## 2. Wilcox (2006) $k$ – $\omega$ model with buoyancy

### 2.1. Turbulence closure model

This study considers incompressible flow in which buoyancy is represented by the Boussinesq approximation. The Reynolds-averaged momentum and temperature transport equations are

$$\frac{\partial U_i}{\partial t} + U_j \frac{\partial U_i}{\partial x_j} = -\frac{\partial P}{\partial x_i} - g_i b(T - T_0) + \frac{\partial}{\partial x_j} \left( \nu \frac{\partial U_i}{\partial x_j} - \overline{u_i u_j} \right), \quad (2.1)$$

$$\frac{\partial T}{\partial t} + U_i \frac{\partial T}{\partial x_i} = Q + \frac{\partial}{\partial x_i} \left( a \frac{\partial T}{\partial x_i} - \overline{\theta u_i} \right), \quad (2.2)$$

where  $U_i$  and  $u_i$  are the mean and fluctuating velocity components,  $T$  and  $\theta$  are the mean and fluctuating temperature,  $x_i$  denotes the Cartesian coordinates, and  $t$  is time.  $P$  is the mean kinematic pressure,  $g_i$  is the gravitational acceleration,  $b$  is the thermal expansion coefficient,  $T_0$  is a reference temperature,  $\nu$  is the kinematic viscosity,  $Q$  is the volumetric heat source per unit heat capacity, and  $a$  is the thermal diffusivity. When a lower wall is present, the value of  $T_0$  merely shifts the hydrostatic reference state and does not affect the fluid motion; for simplicity,  $T_0$  is set to zero. The overbar denotes Reynolds averaging, and  $\overline{u_i u_j}$  and  $\overline{\theta u_i}$  are the Reynolds stress tensor and the turbulent heat flux vector, respectively, modelled using the turbulent-viscosity and gradient-diffusion hypotheses as

$$\overline{u_i u_j} = \frac{2}{3} k \delta_{ij} - 2 \nu_T S_{ij}, \quad \overline{\theta u_i} = -a_T \frac{\partial T}{\partial x_i}, \quad (2.3)$$

where

$$S_{ij} = \frac{1}{2} \left( \frac{\partial U_i}{\partial x_j} + \frac{\partial U_j}{\partial x_i} \right), \quad a_T = \frac{\nu_T}{Pr_T}. \quad (2.4)$$

Here  $S_{ij}$  is the mean strain-rate tensor,  $\nu_T$  is the turbulent viscosity,  $a_T$  is the turbulent thermal diffusivity, and the turbulent Prandtl number is set to  $Pr_T = 0.89$ .

This study analyses the Wilcox (2006)  $k$ – $\omega$  model. The notation for the model variables and constants follows that reference exactly, with only the buoyant terms added. The full set of model equations, including the transport equations for  $k$  and  $\omega$ , is given by:

$$\nu_T = \frac{k}{\tilde{\omega}}, \quad \tilde{\omega} = \max \left\{ \omega, C_{lim} \sqrt{\frac{2 S_{ij} S_{ij}}{\beta^*}} \right\}, \quad (2.5)$$

$$\frac{\partial k}{\partial t} + U_j \frac{\partial k}{\partial x_j} = \mathcal{P} + \mathcal{P}_b - \beta^* k \omega + \frac{\partial}{\partial x_j} \left[ \left( \nu + \sigma^* \frac{k}{\omega} \right) \frac{\partial k}{\partial x_j} \right], \quad (2.6)$$

$$\frac{\partial \omega}{\partial t} + U_j \frac{\partial \omega}{\partial x_j} = \alpha \frac{\omega}{k} (\mathcal{P} + C_{\omega b} \mathcal{P}_b) - \beta_0 f_\beta \omega^2 + \frac{\sigma_d}{\omega} \frac{\partial k}{\partial x_j} \frac{\partial \omega}{\partial x_j} + \frac{\partial}{\partial x_j} \left[ \left( \nu + \sigma \frac{k}{\omega} \right) \frac{\partial \omega}{\partial x_j} \right], \quad (2.7)$$

where the turbulent kinetic energy production terms due to the mean velocity gradient and buoyancy are

$$\mathcal{P} = -\bar{u}_i u_j \frac{\partial U_i}{\partial x_j}, \quad \text{and} \quad \mathcal{P}_b = -g_i b \bar{u}_i. \quad (2.8)$$

The auxiliary relations are

$$\sigma_d = \begin{cases} 0, & \frac{\partial k}{\partial x_j} \frac{\partial \omega}{\partial x_j} \leq 0 \\ \sigma_{do}, & \frac{\partial k}{\partial x_j} \frac{\partial \omega}{\partial x_j} > 0, \end{cases} \quad (2.9)$$

$$f_\beta = \frac{1 + 85\chi_\omega}{1 + 100\chi_\omega}, \quad \chi_\omega = \left| \frac{\mathcal{Q}_{ij} \mathcal{Q}_{jk} S_{ki}}{(\beta^* \omega)^3} \right| \quad (2.10)$$

with

$$\mathcal{Q}_{ij} = \frac{1}{2} \left( \frac{\partial U_i}{\partial x_j} - \frac{\partial U_j}{\partial x_i} \right). \quad (2.11)$$

The closure coefficients are  $C_{lim} = 0.875$ ,  $\beta^* = 0.09$ ,  $\sigma^* = 0.6$ ,  $\alpha = 0.52$ ,  $\beta_0 = 0.0708$ ,  $\sigma = 0.5$ , and  $\sigma_{do} = 0.125$ . In the  $\omega$ -equation, the model constant associated with buoyancy effects is  $C_{\omega b}$ .

At no slip wall, boundary conditions are

$$k = 0, \quad \omega = \frac{6\nu}{\beta_0 n^2} \quad (2.12)$$

where, for a cell-centred discretisation of  $\omega$ ,  $n$  is the wall-normal distance from the wall to the centre of the first off-wall grid cell.

## 2.2. Buoyancy treatment in the scale-determining equation

This subsection reviews how buoyancy effects have been incorporated into the  $\varepsilon$ - and  $\omega$ -equations. Because most previous work is framed within the  $k-\varepsilon$  model, that formulation is first outlined and its relation to the  $k-\omega$  model is then described.

When the standard  $k-\varepsilon$  model of Launder & Sharma (1974) is extended to include buoyant production, it takes the form

$$\nu_T = C_\mu f_\mu \frac{k^2}{\varepsilon}, \quad (2.13)$$

$$\frac{\partial k}{\partial t} + U_j \frac{\partial k}{\partial x_j} = \mathcal{P} + \mathcal{P}_b - \varepsilon - 2\nu \left( \frac{\partial k^{1/2}}{\partial x_j} \frac{\partial k^{1/2}}{\partial x_j} \right) + \frac{\partial}{\partial x_j} \left[ \left( \nu + \frac{\nu_T}{\sigma_k} \right) \frac{\partial k}{\partial x_j} \right], \quad (2.14)$$

$$\frac{\partial \varepsilon}{\partial t} + U_j \frac{\partial \varepsilon}{\partial x_j} = C_{\varepsilon 1} \frac{\varepsilon}{k} (\mathcal{P} + C_{\varepsilon b} \mathcal{P}_b) - C_{\varepsilon 2} f_\varepsilon \frac{\varepsilon^2}{k} + \frac{\partial}{\partial x_j} \left[ \left( \nu + \frac{\nu_T}{\sigma_\varepsilon} \right) \frac{\partial \varepsilon}{\partial x_j} \right], \quad (2.15)$$

with damping functions

$$f_\varepsilon = 1.0 - 0.3 \exp \left[ - \left( \frac{k^2}{\nu \varepsilon} \right)^2 \right], \quad f_\mu = \exp \left[ - \frac{3.4}{1 + 0.02k^2/(\nu \varepsilon)} \right]. \quad (2.16)$$

The closure coefficients are  $C_{\varepsilon 1} = 1.44$ ,  $C_{\varepsilon 2} = 1.92$ ,  $C_\mu = 0.09$ ,  $\sigma_k = 1.0$ , and  $\sigma_\varepsilon = 1.3$ , with  $k = \varepsilon = 0$  at no-slip walls.

To establish correspondence with the  $k$ - $\omega$  formulation, the  $\varepsilon$ -equation can be recast by introducing  $\varepsilon = \beta^* k \omega$  (Pope 2000). Assuming  $\nu_T \gg \nu$ , so that molecular viscosity is negligible and  $f_\mu = f_\varepsilon = 1$ , substitution yields

$$\begin{aligned} \frac{\partial \omega}{\partial t} + U_j \frac{\partial \omega}{\partial x_j} &= (C_{\varepsilon 1} - 1) \frac{\omega}{k} \mathcal{P} + (C_{\varepsilon 1} C_{\varepsilon b} - 1) \frac{\omega}{k} \mathcal{P}_b - (C_{\varepsilon 2} - 1) \omega^2 \\ &\quad + \frac{C_\mu}{\beta^*} \left( \frac{1}{\sigma_\varepsilon} - \frac{1}{\sigma_k} \right) \left( \frac{1}{k} \frac{\partial k}{\partial x_j} \frac{\partial k}{\partial x_j} + \frac{\partial^2 k}{\partial x_j \partial x_j} \right) \\ &\quad + \frac{C_\mu}{\beta^*} \left( \frac{1}{\sigma_\varepsilon} + \frac{1}{\sigma_k} \right) \frac{1}{\omega} \frac{\partial k}{\partial x_j} \frac{\partial \omega}{\partial x_j} + \frac{\partial}{\partial x_j} \left[ \frac{\nu_T}{\sigma_\varepsilon} \frac{\partial \omega}{\partial x_j} \right]. \end{aligned} \quad (2.17)$$

with the approximate correspondence

$$\frac{C_{\varepsilon 1} C_{\varepsilon b} - 1}{C_{\varepsilon 1} - 1} \approx \frac{(\alpha + 1) C_{\varepsilon b} - 1}{\alpha} \approx C_{\omega b}. \quad (2.18)$$

In most prior studies, discussions of buoyant production have been anchored to the  $k$ - $\varepsilon$  framework. As noted in the Introduction, there is no universally accepted standard for  $C_{\varepsilon b}$ ; reported values range approximately from 0 to 1 (Hanjalić & Launder 2011; Burchard 2007; Henkes *et al.* 1991; Peng & Davidson 1999; Hanjalić & Vasić 1993). The proposal of Markatos & Pericleous (1984) to omit the buoyancy contribution corresponds to  $C_{\varepsilon b} = 0$ . An equally common practice is to treat shear and buoyant production on the same footing, corresponding to  $C_{\varepsilon b} = 1$  (Ince & Launder 1989; Craft *et al.* 1996; Choi & Kim 2012). Within this spectrum, the reference work of Rodi (1980) suggested that  $C_{\varepsilon b}$  should approach unity in vertical buoyant shear layers and vanish in horizontal layers. Along similar lines, Henkes *et al.* (1991) proposed a velocity-ratio form for the buoyancy coefficient,  $C_{\varepsilon b} = \tanh |v/u|$ , where  $v$  denotes the velocity component aligned with gravity and  $u$  the component perpendicular to it. Another approach by Rodi (1987) recommended  $C_{\varepsilon b} = 1$  for unstable stratification and near zero for stable layers, a prescription based on an optimisation for an unstable shear flow at a reduced Froude number of 0.9 (defined as the ratio of the maximum shear-velocity difference to the buoyancy free-fall velocity) reported by Viollet (1987).

These empirical prescriptions have propagated into widely used turbulence solvers, both open-source and commercial. OpenFOAM (OpenCFD Ltd. 2025) adopts  $C_{\varepsilon b} = 1$  by default, whereas Fluent (ANSYS 2021b) uses  $C_{\varepsilon b} = 0$  and offers the alternative  $C_{\varepsilon b} = \tanh |v/u|$ , following Henkes *et al.* (1991). In CFX (ANSYS 2021a), the buoyancy source term in the  $\omega$ -equation is implemented as

$$\frac{\omega}{k} [(\alpha + 1) \max(\mathcal{P}_b, 0) f_\phi - \mathcal{P}_b],$$

which corresponds to  $C_{\omega b} = 1$  for  $\mathcal{P}_b > 0$  and  $C_{\omega b} \approx -2$  for  $\mathcal{P}_b < 0$ , with the default setting  $f_\phi = 1$ . This formulation is identical to the recommendation of Rodi (1987) for  $C_{\varepsilon b}$ , as related through Eq. (2.18). An alternative is provided as  $f_\phi = \sin(\phi)$ , where  $\phi$  denotes the angle between the flow direction and gravity, again following Henkes *et al.* (1991).

However, both Henkes' proposal and the introduction of  $\sin(\phi)$  in CFX violate Galilean invariance. A simple counterexample arises by shifting the reference frame with velocity  $v'$  in the direction of gravity; in this case  $C_{\varepsilon b} = \tanh |(v - v')/u|$  changes its value. Even if this were interpreted as an absolute-frame velocity relative to a stationary wall, it would imply that a locally defined model equation depends on a remote boundary without

explicit specification. From any viewpoint, such approaches undermine the completeness of two-equation closures.

Across the cited studies (Rodi 1980; Markatos & Pericleous 1984; Rodi 1987; Viollet 1987; Henkes *et al.* 1991; Hanjalić & Vasić 1993; Peng & Davidson 1999; Burchard 2007; Hanjalić & Launder 2011, 2021), it has been repeatedly noted that, despite various empirical proposals, no firm theoretical criterion exists for incorporating buoyancy effects into the scale-determining equations. Moreover, even if buoyancy effects are introduced analogously in the  $k$ - $\varepsilon$  and  $k$ - $\omega$  models, there is no guarantee that the resulting behaviour will remain consistent between the two formulations. These limitations motivate the analytical framework developed in the following sections.

### 3. Analytical solution in Rayleigh–Bénard convection

The aim of this analysis is to establish how the standard  $k$ - $\omega$  model predicts the Nusselt number as a function of the Rayleigh and Prandtl numbers in a buoyancy-driven flow. As mentioned in §1, a one-dimensional Rayleigh–Bénard configuration is selected as a testbed for the analysis, in which all mean quantities depend solely on the vertical coordinate  $z$  and the mean velocity is zero. In this configuration, the turbulent kinetic energy budget is governed solely by buoyant production, thereby isolating the role of the buoyancy term in the  $\omega$  equation.

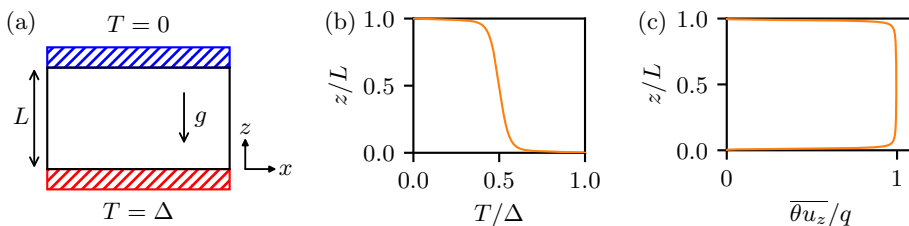


Figure 1. (a) Rayleigh–Bénard convection setup, (b) mean temperature distribution, and (c) turbulent heat flux.

Figure 1(a) shows the Rayleigh–Bénard configuration and its boundary conditions. The walls are no-slip and isothermal, with  $T = 0$  at  $z = L$  and  $T = \Delta$  at  $z = 0$ . The dimensionless control parameters are the Rayleigh and Prandtl numbers, defined as  $Ra = gb\Delta L^3/(va)$  and  $Pr = v/a$ . The Nusselt number is defined as

$$Nu = \frac{qL}{a\Delta}, \quad q = -a \frac{dT}{dz} + \overline{\theta u_z}, \quad (3.1)$$

where the total heat flux  $q$  is the sum of the conductive and turbulent contributions and remains constant along the vertical direction. Figures 1(b,c) illustrate how the mean temperature and turbulent heat flux vary with height. Gravity acts in the negative  $z$  direction, with  $U_i = 0$ ,  $dT/dz < 0$ , and  $\overline{\theta u_z} > 0$ .

In this study, the kinetic and thermal boundary-layer thicknesses,  $\lambda_v$  and  $\lambda_a$ , are defined as the locations where  $v = v_T$  and  $a = a_T$ , respectively. Because the diffusion terms in the  $k$ - and  $\omega$ -equations depend on  $v$  and  $v_T$ , the contrast between their wall and bulk distributions must be interpreted separately relative to  $\lambda_v$ . In contrast,  $\lambda_a$  characterises the distribution of heat transfer: within  $\lambda_a$ , the conductive approximation  $q \approx -adT/dz$  holds adjacent to the wall, whereas outside  $\lambda_a$  the turbulent relation  $q \approx \overline{\theta u_z}$  applies.

### 3.1. Distribution of $\omega$

The distribution of  $\omega$  is first established. Owing to the symmetry of the domain, only the half region  $0 \leq z \leq L/2$  is considered. For the analytical derivation, the governing equation is simplified uniformly under the condition  $\nu \gg \nu_T$  in the region  $z \leq \lambda_\nu$ , whereas in the region  $z \geq \lambda_\nu$ , it is simplified under the opposite condition  $\nu \ll \nu_T$ . Under these assumptions, the resulting  $\omega$  distributions are continuous at the interface  $z = \lambda_\nu$ , although their spatial gradients are discontinuous.

Close to the wall ( $z \leq \lambda_\nu$ ), the distribution of  $\omega$  is fixed by the boundary condition of the model (Wilcox 2006):

$$\omega = \frac{6\nu}{\beta_0 z^2}. \quad (3.2)$$

This expression can also be obtained from the  $\omega$ -equation by balancing the sink term with the viscous diffusion term.

In the bulk region,  $\lambda_\nu \leq z \leq L/2$ , the distribution of  $\omega$  is determined under the approximation  $\nu_T \gg \nu$ . In the  $k$ -equation for the bulk, it is assumed that the production of  $k$  is balanced with dissipation as  $\mathcal{P}_b = \beta^* k \omega$ . The heat balance (Eq. 3.1) gives

$$\mathcal{P}_b = g b \overline{\theta u_z} = -g b a T \frac{dT}{dz} = \frac{q b q}{1 + a P r_T / \nu_T}, \quad (3.3)$$

and  $\mathcal{P}_b = \beta^* k \omega$  reduces to

$$\frac{q b q}{1 + a P r_T / \nu_T} = \beta^* k \omega. \quad (3.4)$$

Using  $\nu_T = k/\omega$ , this can be written as

$$k = \frac{g b q}{\beta^* \omega} - P r_T a \omega. \quad (3.5)$$

Since production and dissipation balance in the  $k$ -equation but not in the  $\omega$ -equation, diffusion must be retained in the latter. The  $\omega$ -equation in the bulk then becomes

$$0 = \alpha \frac{\omega}{k} C_{\omega b} \frac{q b q}{1 + a P r_T / \nu_T} - \beta_0 \omega^2 + \frac{d}{dz} \left( \sigma \frac{k}{\omega} \frac{d\omega}{dz} \right). \quad (3.6)$$

Substituting  $k$  from Eq. (3.5), this leads to

$$\frac{d}{dz} \left[ \left( \frac{1}{\omega^2} - \frac{\beta^* P r_T a}{g b q} \right) \frac{d\omega}{dz} \right] = \frac{\beta^*}{\sigma g b q} (\beta_0 - \alpha \beta^* C_{\omega b}) \omega^2. \quad (3.7)$$

The value of  $\omega$  is largest at the wall and decreases toward the domain centre. Hence the right-hand side must be positive, which imposes a constraint on  $C_{\omega b}$ :

$$C_{\omega b} < \frac{\beta_0}{\alpha \beta^*} = 1.52 \quad \text{for } \mathcal{P}_b > 0. \quad (3.8)$$

The  $\omega$ -equation can be written in non-dimensional form as

$$\frac{d^2 \tau}{dz^{*2}} - K \frac{d^2}{dz^{*2}} \left( \frac{1}{\tau} \right) = -\frac{A}{\tau^2}, \quad (3.9)$$

where

$$\tau = \frac{\nu}{L^2 \omega}, \quad z^* = \frac{z}{L}, \quad (3.10)$$

$$A = \frac{\beta^*}{\sigma} (\beta_0 - \alpha \beta^* C_{\omega b}) \Pr^2 \text{Nu}^{-1} \text{Ra}^{-1}, \quad (3.11)$$

$$K = \Pr_T \beta^* \text{Nu}^{-1} \text{Ra}^{-1} \Pr. \quad (3.12)$$

The constant  $K$  arises from the  $a \Pr_T / \nu_T$  term in the bulk expression of  $\mathcal{P}_b$  (Eq. 3.3). In the asymptotic limit  $z \gg \lambda_\nu$ , where  $q \approx \theta u_z$ , this contribution vanishes and hence  $K \approx 0$ .

The corresponding boundary conditions are

$$\tau = \tau_\nu = \frac{\beta_0}{6} \left( \frac{\lambda_\nu}{L} \right)^2 \quad \text{at} \quad z^* = \frac{\lambda_\nu}{L}, \quad (3.13)$$

$$\frac{d\tau}{dz^*} = 0 \quad \text{at} \quad z^* = \frac{1}{2}. \quad (3.14)$$

where  $\tau_\nu$  denotes the value of  $\tau$  at  $z^* = \lambda_\nu / L$ .

Equation (3.9) is then solved to obtain an analytical solution. When  $K = 0$ , the equation admits a simple closed-form solution, whereas for  $K \neq 0$  the expression becomes considerably more complex. Since the aim of this study is to gain structural insight into the model through a tractable analytical formulation, the analysis is restricted to the case  $K = 0$ . From Eq. (3.12),  $K \approx 0$  is satisfied when  $\text{Ra}$  is sufficiently large and  $\Pr$  is not excessive.

Multiplying the differential equation for  $\tau$  (Eq. 3.9) by  $d\tau/dz^*$  and integrating under the boundary conditions gives

$$\left( \frac{d\tau}{dz^*} \right)^2 = 2A \left( \frac{1}{\tau} - \frac{1}{\tau_c} \right), \quad (3.15)$$

where  $\tau_c$  denotes the value of  $\tau$  at the centre of the domain ( $z^* = 1/2$ ).

Integration of this relation gives

$$z^* = \frac{1}{2} - \sqrt{\frac{\tau_c^3}{2A}} \left[ \arccos \left( \sqrt{\frac{\tau}{\tau_c}} \right) + \sqrt{\frac{\tau}{\tau_c} \left( 1 - \frac{\tau}{\tau_c} \right)} \right], \quad (3.16)$$

which satisfies  $z^* = 0.5$  at  $\tau = \tau_c$ .

The value of  $\tau_c$  follows from substituting  $\tau = \tau_\nu$  at  $z^* = \lambda_\nu / L$ . When the boundary layer is thin,  $\omega$  is very large near the wall and much smaller in the core, so that  $\tau_\nu / \tau_c \ll 1$ . Expanding the arccos and square-root terms in a Taylor series then gives

$$\frac{\lambda_\nu}{L} = \frac{1}{2} - \sqrt{\frac{\tau_c^3}{2A}} \left[ \frac{\pi}{2} - \frac{2}{3} \left( \frac{\tau_\nu}{\tau_c} \right)^{3/2} + \dots \right], \quad (3.17)$$

$$\tau_c = \left( \frac{2A}{\pi^2} \right)^{1/3} \left[ 1 - \frac{4}{3} \frac{\lambda_\nu}{L} + \frac{4}{9} \sqrt{\frac{2}{A}} \tau_\nu^{3/2} + \dots \right]. \quad (3.18)$$

Thus,  $\omega$  attains its minimum value at  $z = L/2$ , given by  $\nu L^{-2} \tau_c^{-1}$ .

### 3.2. Distribution of $k$

In the bulk region ( $\lambda_\nu \leq z \leq L/2$ ), the distribution of  $k$  follows directly from Eq. (3.5) by substituting the previously obtained distribution of  $\omega$  (Eq. 3.16). In the near-wall region ( $z \leq \lambda_\nu$ ), similar to the  $\omega$  distribution, the  $k$  distribution is determined by the intrinsic

behaviour of the  $k-\omega$  model (Wilcox 2006). The  $k$ -equation reduces to a balance between dissipation and diffusion:

$$\beta^* k \omega = \nu \frac{d^2 k}{dz^2}, \quad (3.19)$$

and substitution of  $\omega = 6\nu/(\beta_0 z^2)$  gives

$$\frac{6\beta^*}{\beta_0} \frac{k}{z^2} = \frac{d^2 k}{dz^2}. \quad (3.20)$$

Assuming a power-law form  $k \propto z^P$  yields

$$P = \frac{1}{2} + \sqrt{\frac{6\beta^*}{\beta_0} + \frac{1}{4}} \approx 3.307. \quad (3.21)$$

Thus, for  $z \leq \lambda_\nu$ , the near-wall distribution of  $k$  is approximated as

$$k = k_\nu \left( \frac{z}{\lambda_\nu} \right)^P, \quad (3.22)$$

where  $k_\nu$  denotes the value of  $k$  at  $z = \lambda_\nu$ .  $k_\nu$  is obtained by enforcing continuity between the near-wall and bulk distributions at  $z = \lambda_\nu$ , which gives

$$k_\nu = \frac{gbq}{\beta^*} \frac{\beta_0 \lambda_\nu^2}{6\nu}. \quad (3.23)$$

### 3.3. Boundary-layer thicknesses

By substituting the values of  $k$  and  $\omega$  at  $z = \lambda_\nu$  obtained from Eqs. (3.2) and (3.23), the turbulent viscosity  $\nu_T = k/\omega$  at this point is

$$\nu_T = \frac{gbq}{\beta^*} \left( \frac{6\nu}{\beta_0 \lambda_\nu^2} \right)^{-2}. \quad (3.24)$$

Applying the defined condition  $\nu = \nu_T$  at  $z = \lambda_\nu$  gives the estimate

$$\frac{\lambda_\nu}{L} = \left( \frac{36\beta^*}{\beta_0^2} \right)^{1/4} \text{Nu}^{-1/4} \text{Ra}^{-1/4} \text{Pr}^{1/2}, \quad (3.25)$$

and hence

$$\tau_\nu = \beta^{*1/2} \text{Nu}^{-1/2} \text{Ra}^{-1/2} \text{Pr}, \quad (3.26)$$

which represents the value of  $\omega = \nu/(L^2 \tau_\nu)$  at  $z = \lambda_\nu$ .

When  $\text{Pr} \geq \text{Pr}_T$ , and hence  $\lambda_a \leq \lambda_\nu$ , the thermal boundary-layer thickness is estimated from  $a = a_T$  at  $z = \lambda_a$ , using the near-wall distribution of  $\nu_T/\nu$ :

$$\frac{a_T}{a} = \frac{\text{Pr}}{\text{Pr}_T} \frac{\nu_T}{\nu} = \frac{\text{Pr}}{\text{Pr}_T} \left( \frac{\lambda_a}{\lambda_\nu} \right)^{P+2} = 1, \quad (3.27)$$

where  $P = 3.307$ . It then follows that

$$\frac{\lambda_a}{L} = \left( \frac{36\beta^*}{\beta_0^2} \right)^{1/4} \text{Pr}_T^{1/(P+2)} \text{Nu}^{-1/4} \text{Ra}^{-1/4} \text{Pr}^{P/(2P+4)}. \quad (3.28)$$

On the other hand, when  $Pr \leq Pr_T$ , so that  $\lambda_a \geq \lambda_v$ ,  $\lambda_a$  should be derived from the bulk distribution of  $\omega$ . The condition  $a = a_T$ , with  $\nu_T = k/\omega \approx gbq\beta^{*-1}(L^2\tau_a/\nu)^2$ , yields

$$\tau_a = \beta^{*1/2} Pr_T^{1/2} Nu^{-1/2} Ra^{-1/2} Pr^{1/2}, \quad (3.29)$$

where  $\tau_a$  is the value of  $\tau$  at  $z = \lambda_a$ . Assuming  $\tau_a \ll \tau_c$ , a Taylor expansion of the  $\tau-z^*$  relation (Eq. 3.16) gives

$$\frac{\lambda_a}{L} \approx \frac{1}{2} - \sqrt{\frac{\tau_c^3}{2A}} \left[ \frac{\pi}{2} - \frac{2}{3} \left( \frac{\tau_a}{\tau_c} \right)^{3/2} + \dots \right], \quad (3.30)$$

and  $\lambda_a$  for  $Pr \leq Pr_T$  is obtained as

$$\begin{aligned} \frac{\lambda_a - \lambda_v}{L} &\approx \frac{2}{3} \sqrt{\frac{\tau_c^3}{2A}} \left[ \left( \frac{\tau_a}{\tau_c} \right)^{3/2} - \left( \frac{\tau_v}{\tau_c} \right)^{3/2} \right] \\ &= \frac{\sqrt{2}}{3} \frac{\sigma^{1/2}}{\alpha^{1/2} \beta^{*1/4}} \left( \frac{\beta_0}{\alpha \beta^*} - C_{\omega b} \right)^{-1/2} \left( Pr_T^{3/4} - Pr^{3/4} \right) Nu^{-1/4} Ra^{-1/4} Pr^{-1/4}. \end{aligned} \quad (3.31)$$

By substituting the expressions for the boundary-layer thicknesses derived above, the distributions of  $\omega$  and  $k$  can be expressed as functions of  $Ra$ ,  $Pr$ , and  $Nu$ .

### 3.4. Temperature profile

The temperature profile is analysed separately in the near-wall region ( $z \leq \lambda_v$ ) and in the bulk region ( $\lambda_v \leq z \leq L/2$ ), providing the basis for establishing the relation among  $Nu$ ,  $Ra$ , and  $Pr$  discussed in §3.5. The associated heat balance is governed by the thermal boundary-layer thickness  $\lambda_a$ . For  $z > \lambda_a$ , the heat flux can be approximated by the turbulent relation  $q \approx \bar{\theta}u_z$ , whereas for  $z < \lambda_a$  the effect of molecular thermal diffusivity  $a$  must also be taken into account.

#### 3.4.1. Near-wall contribution

The near-wall temperature rise across the kinetic boundary-layer thickness,  $\Delta_{BL}$ , is first evaluated as

$$\begin{aligned} \frac{\Delta_{BL}}{\Delta} &= -\frac{1}{\Delta} \int_0^{\lambda_v} \frac{dT}{dz} dz = Nu \left( \frac{\lambda_v}{L} \right) \int_0^1 \frac{1}{1 + a_T/a} dz' \\ &= \left( \frac{36\beta^*}{\beta_0^2} \right)^{1/4} Nu^{3/4} Ra^{-1/4} Pr^{1/2} \int_0^1 \frac{1}{1 + (Pr/Pr_T)z'^{p'}} dz', \end{aligned} \quad (3.32)$$

where  $p' = p + 2 = 5.307$ ,  $a_T/a = (Pr/Pr_T)(z/\lambda_v)^{p+2}$ , and  $z' = z/\lambda_v$ .

The integral in the second line approaches unity when  $Pr/Pr_T \ll 1$ . For  $Pr/Pr_T \gg 1$ , its asymptotic value can be obtained by applying the variable transformation  $\eta = (Pr/Pr_T)z'^{p'}$ , yielding (Arfken *et al.* 2013):

$$\begin{aligned} \int_0^1 \frac{1}{1 + (Pr/Pr_T)z'^{p'}} dz' &\approx \frac{1}{p'} \left( \frac{Pr}{Pr_T} \right)^{-1/p'} \int_0^\infty \frac{\eta^{\frac{1}{p'}-1}}{1 + \eta} d\eta \\ &= \frac{\pi}{p' \sin(\pi/p')} \left( \frac{Pr}{Pr_T} \right)^{-1/p'}. \end{aligned} \quad (3.33)$$

On the basis of the asymptotic behaviour described above, the integral can be approximated by a simple algebraic function,

$$\left(1 + 0.7535(Pr/Pr_T)^{0.9338}\right)^{-1/(0.9338p')},$$

which satisfies the asymptotic limits for both  $Pr/Pr_T \ll 1$  and  $Pr/Pr_T \gg 1$ . This approximation yields a maximum relative error of 0.2% over the range  $10^{-4} \leq (Pr/Pr_T) \leq 10^4$ .

Combining the above results, the near-wall temperature rise is expressed as

$$\frac{\Delta_{BL}}{\Delta} = 4.506 Nu^{3/4} Ra^{-1/4} Pr^{1/2} \left[1 + 0.7535 \left(\frac{Pr}{Pr_T}\right)^{0.9338}\right]^{-1/(0.9338p')}. \quad (3.34)$$

### 3.4.2. Bulk contribution for $Pr \geq Pr_T$

The bulk contribution,  $\Delta_{bulk}$ , is now considered. For  $Pr \geq Pr_T$ , the approximation  $\overline{\theta u_z} \approx q$  holds throughout the bulk region, where  $z \geq \lambda_v \geq \lambda_a$ . From the heat balance equation, the temperature gradient is expressed as

$$\frac{dT}{dz} \approx -\frac{q}{\nu_T/Pr_T} = -\frac{\Delta}{L} \beta^* Pr_T Ra^{-1} Pr \frac{1}{\tau^2}. \quad (3.35)$$

Integration between  $z = \lambda_v$  and  $z = L/2$  then gives the bulk temperature rise:

$$\begin{aligned} \frac{\Delta_{bulk}}{\Delta} &\approx \frac{1}{\Delta} \int_{\lambda_v}^{L/2} \frac{q}{\nu_T/Pr_T} dz = \beta^* Pr_T Ra^{-1} Pr \int_{\lambda_v/L}^{1/2} \frac{1}{\tau^2} d\tau^* \\ &= \beta^* Pr_T Ra^{-1} Pr \int_{\tau_v}^{\tau_c} \frac{1}{\tau^2} \left[2A\left(\frac{1}{\tau} - \frac{1}{\tau_c}\right)\right]^{-1/2} d\tau \\ &= \frac{\sqrt{2}\sigma^{1/2}\beta^{*1/4}}{(\beta_0 - \alpha\beta^*C_{\omega b})^{1/2}} \left(1 - \frac{\tau_v}{\tau_c}\right)^{1/2} Nu^{3/4} Ra^{-1/4} Pr^{-1/2} \\ &\approx 2.532 \left(\frac{\beta_0}{\alpha\beta^*} - C_{\omega b}\right)^{-1/2} Pr_T Nu^{3/4} Ra^{-1/4} Pr^{-1/2}. \end{aligned} \quad (3.36)$$

The final expression is obtained by applying the assumption  $\tau_v/\tau_c \ll 1$ .

### 3.4.3. Bulk contribution for $Pr \leq Pr_T$

For  $Pr \leq Pr_T$ , the ordering  $\lambda_v \leq \lambda_a$  holds. In the region  $\lambda_v \leq z \leq \lambda_a$ , the total thermal diffusivity  $a + \nu_T/Pr_T$  is less than  $2a$ , so that the approximation  $\nu_T/Pr_T \approx 0$  is adopted, whereas for  $z > \lambda_a$  it is assumed that  $\nu_T/Pr_T \gg a$ . This approximation modifies only the prefactor of the power law while leaving the exponent unchanged, thereby justifying its use in deriving analytical scaling laws.

The bulk temperature rise is then expressed as

$$\frac{\Delta_{bulk}}{\Delta} \approx \frac{1}{\Delta} \int_{\lambda_v}^{\lambda_a} \frac{q}{a} dz + \frac{1}{\Delta} \int_{\lambda_a}^{L/2} \frac{q}{\nu_T/Pr_T} dz. \quad (3.37)$$

Using the expressions for  $\tau_a$  and  $\lambda_a$  in Eqs. (3.29) and (3.31), it follows that

$$\begin{aligned} \frac{1}{4} \int_{\lambda_\nu}^{\lambda_a} \frac{q}{a} dz &= Nu \left( \frac{\lambda_a - \lambda_\nu}{L} \right) \\ &\approx \frac{\sqrt{2}}{3} \frac{\sigma^{1/2}}{\alpha^{1/2} \beta^{*1/4}} \left( \frac{\beta_0}{\alpha \beta^*} - C_{\omega b} \right)^{-1/2} \left( Pr_T^{3/4} - Pr^{3/4} \right) Nu^{3/4} Ra^{-1/4} Pr^{-1/4}, \end{aligned} \quad (3.38)$$

and

$$\begin{aligned} \frac{1}{4} \int_{\lambda_a}^{L/2} \frac{q}{\nu_T/Pr_T} dz &= \beta^* Pr_T Ra^{-1} Pr \left( \frac{2}{A\tau_a} \right)^{1/2} \left( 1 - \frac{\tau_a}{\tau_c} \right)^{1/2} \\ &\approx \frac{\sqrt{2}\sigma^{1/2}}{\beta^{*1/4} \alpha^{1/2}} Pr_T^{3/4} \left( \frac{\beta_0}{\alpha \beta^*} - C_{\omega b} \right)^{-1/2} Nu^{3/4} Ra^{-1/4} Pr^{-1/4}. \end{aligned} \quad (3.39)$$

By summing the two contributions obtained above, the total bulk temperature rise becomes

$$\frac{\Delta_{bulk}}{4} \approx 2.532 \left( \frac{\beta_0}{\alpha \beta^*} - C_{\omega b} \right)^{-1/2} \left( \frac{4}{3} Pr_T^{3/4} - \frac{1}{3} Pr^{3/4} \right) Nu^{3/4} Ra^{-1/4} Pr^{-1/4}. \quad (3.40)$$

### 3.5. Dependence of $Nu$ on $Ra$ and $Pr$

The total temperature rise across the half-domain satisfies  $\Delta/2 = \Delta_{BL} + \Delta_{bulk}$ . By combining the near-wall and bulk contributions obtained in Eqs. (3.34), (3.36), and (3.40), the resulting relation can be expressed as

$$\begin{aligned} \frac{1}{2} &\approx 4.506 Nu^{3/4} Ra^{-1/4} Pr^{1/2} \left[ 1 + 0.7535 \left( \frac{Pr}{Pr_T} \right)^{0.9338} \right]^{-1/(0.9338p')} \\ &+ 2.532 C'_{\omega b}^{-1/2} Nu^{3/4} Ra^{-1/4} Pr_T^{1/2} f \left( \frac{Pr}{Pr_T} \right), \end{aligned} \quad (3.41)$$

with

$$C'_{\omega b} = \frac{\beta_0}{\alpha \beta^*} - C_{\omega b} > 0, \quad (3.42)$$

and

$$f(s) = \begin{cases} \frac{4}{3}s^{-1/4} - \frac{1}{3}s^{1/2}, & 0 < s < 1 \\ s^{-1/2}, & s \geq 1. \end{cases} \quad (3.43)$$

The bridging function  $f(s)$  is continuous and differentiable at  $s = 1$ , ensuring a smooth crossover between the regimes.

From Eq. (3.41), the asymptotic dependence of  $Nu$  on  $Ra$  and  $Pr$  is

$$Nu \sim \begin{cases} Ra^{1/3} Pr^{1/3}, & Pr \ll 1 \\ Ra^{1/3} Pr^{-2/3+4/(3p')}, & Pr \gg 1. \end{cases} \quad (3.44)$$

Here, for  $Pr \gg 1$ , the exponent of  $Pr$  evaluates to  $-0.4154$ , with  $p' = 5.307$ .

The resulting  $Nu$  dependence on  $Ra$  and  $Pr$  predicted by the standard model exhibits a quantitative deviation from experimental observations. A detailed comparison with

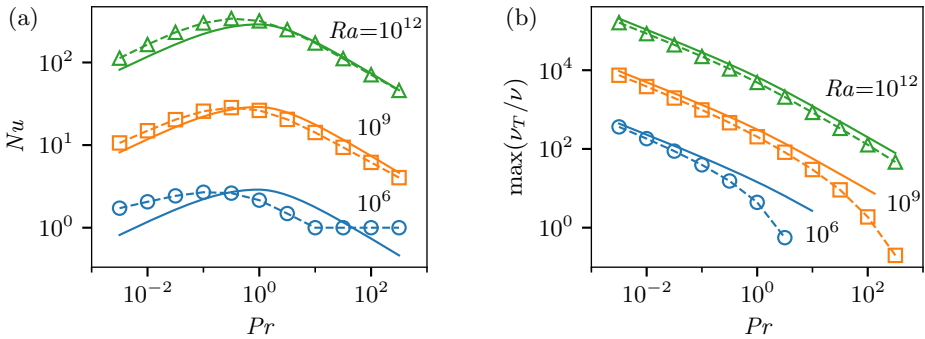


Figure 2. (a) Nusselt number and (b) maximum ratio of turbulent viscosity to kinematic viscosity as functions of the Prandtl number. Circles, squares, and triangles with dashed lines indicate simulation results for  $Ra = 10^6$ ,  $10^9$ , and  $10^{12}$ , respectively. Solid lines denote the analytical prediction.

experiments, along with a new correction proposed to address this discrepancy, is presented in §4.

### 3.6. Validation with simulation

The analytical solution derived in §3.1–3.5 is evaluated against one-dimensional simulations. All simulations are performed for  $C_{\omega b} = 1$ , a baseline value commonly adopted in the literature and used here to establish reference behaviour prior to calibration. The governing equations are solved using the steady-state solver `buoyantSimpleFoam` of the open-source package OpenFOAM (OpenCFD Ltd. 2025). The  $k-\omega$  formulation in OpenFOAM differs slightly from that of Wilcox (2006); therefore, the accurate form is implemented following the recommendations of NASA Langley Research Center (2024) and Gomez *et al.* (2014), with buoyant production included explicitly. All analytical results are determined solely by the prescribed  $Ra$  and  $Pr$ , with  $Nu$  from Eq. (3.41) providing the basis for all dependent quantities.

Figure 2(a) shows that the analytical prediction of  $Nu$  as a function of  $Ra$  and  $Pr$  agrees closely with the simulation results for  $Ra = 10^9$  and  $10^{12}$  across  $10^{-2.5} \leq Pr \leq 10^{2.5}$ . At  $Ra = 10^6$  the deviation arises from the low value of  $Nu$  close to unity, so that the thin-boundary-layer assumption is no longer valid. For  $Pr = 1$ , the simulations yield  $Nu \sim Ra^{0.35}$  over  $10^6 \leq Ra \leq 10^{12}$ , giving an effective scaling exponent slightly larger than  $1/3$  since the simulated  $Nu$  values are lower than the analytical prediction at the lowest  $Ra$ . The predicted maximum of  $v_T/v$ , shown in figure 2(b) and located at  $z = L/2$ , is also consistent with the simulations except when  $v_T$  is not sufficiently greater than  $v$ . The analytical results for  $v_T/v$  is obtained from Eqs. (3.5), (3.10), and (3.18).

Comparisons for the boundary-layer and temperature scales are presented in figure 3. The analytical expressions for  $\lambda_v$  (figure 3a; Eq. 3.25) and  $\lambda_a$  (figure 3b; Eqs. 3.28, 3.31) agree well with the simulations across the entire range investigated. The analytical near-wall temperature  $\Delta_{BL}/\Delta$  (Eq. 3.34) depends solely on  $Pr$  once  $Nu \sim Ra^{1/3}$  is substituted, and figure 3(c) confirms that this relation remains valid and becomes increasingly accurate as  $Ra$  increases. At  $z = \lambda_a$ , the temperature (figure 3d) exceeds  $\Delta_{BL}$  substantially for  $Pr \ll Pr_T$ , as the additional rise of approximately  $q(\lambda_a - \lambda_v)/a$  relative to  $\Delta_{BL}$  is consistent with the discussion in §3.4.3.

The  $\omega$  distributions at  $Ra = 10^{12}$  (figure 4) are well reproduced by the analytical forms, exhibiting the expected change in slope at  $z = \lambda_v$  (§3.1) for both small ( $Pr = 10^{-2}$ ; figure 4a) and large  $Pr$  ( $Pr = 10^2$ ; figure 4b). Minor discrepancies at the smallest  $z$  arise because the singular distribution  $\omega = 6\nu/(\beta_0 z^2)$  is implemented numerically as the fixed

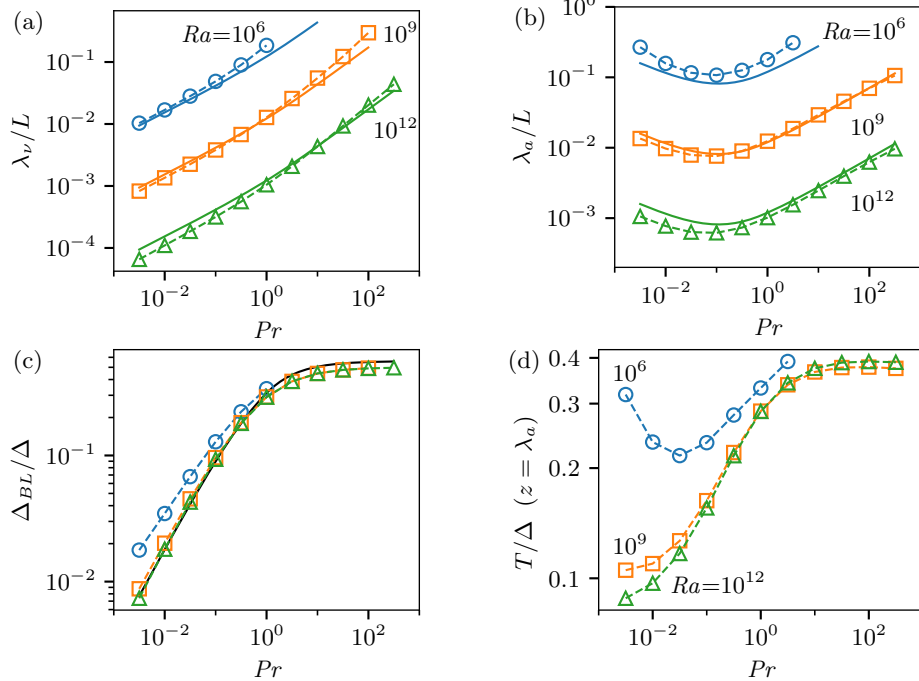


Figure 3. (a) Kinetic and (b) thermal boundary-layer thicknesses, (c) temperature difference across the kinetic boundary layer, and (d) temperature difference across the thermal boundary layer as functions of Prandtl number. Circles, squares, and triangles with dashed lines denote simulation results for  $Ra = 10^6$ ,  $10^9$ , and  $10^{12}$ , respectively. Solid lines represent the analytical relation.

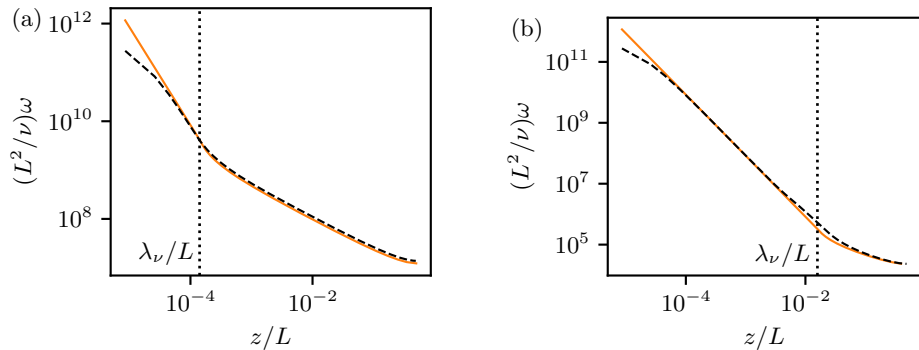


Figure 4. Distribution of  $\omega$  at  $Ra = 10^{12}$  for (a)  $Pr = 10^{-2}$  and (b)  $Pr = 10^2$ . Dashed lines denote simulation results, and solid lines denote the analytical relation. Vertical dotted lines mark the analytical kinetic boundary-layer thicknesses.

value  $\omega = 6\nu/(\beta_0 n^2)$  at the wall, where  $n$  denotes the distance to the first cell centre (Eq. 2.12). In summary, the analytical framework reproduces the simulation results with high accuracy, establishing a consistent foundation for the buoyancy corrections in §4.

#### 4. Formulation and calibration of buoyant corrections

The analytical relation for  $Nu$  (Eq. 3.41) depends not only on the control parameters  $Ra$  and  $Pr$ , but also on the model constants. If  $Pr_T$  and  $C_{\omega b}$  are treated as fixed, the model

cannot alter the asymptotic  $Nu$ – $Ra$ – $Pr$  relations given by Eq. (3.44). To enable calibration, these quantities must therefore be expressed as dimensionless functions, analogous to the auxiliary functions employed in the standard  $k$ – $\omega$  formulations.

The calibration draws upon complementary datasets that collectively span wide ranges of  $Ra$  and  $Pr$ . The plate experiments of Niemela *et al.* (2000) established  $Nu \sim Ra^{0.31}$  over  $10^6 \leq Ra \leq 10^{17}$ , providing a benchmark  $Ra$ -scaling. Three-dimensional DNS studies revealed  $Pr$  dependences of  $Nu \sim Pr^{0.14}$  at  $Ra = 6 \times 10^5$  for  $0.022 \leq Pr \leq 0.7$  (Verzicco & Camussi 1999), and  $Nu \sim Pr^{0.18}$  at  $Ra = 10^6$  for  $0.001 \leq Pr \leq 1$  (Pandey *et al.* 2022). At higher  $Pr$ , the simulations of Li *et al.* (2021) showed an almost  $Pr$ -independent behaviour,  $Nu \sim Pr^{-0.02}$ , for  $11.7 \leq Pr \leq 650.7$  and  $6.0 \times 10^8 \leq Ra \leq 3.0 \times 10^{10}$ . These findings are broadly consistent with the theoretical prediction of Grossmann & Lohse (2000), which yields  $Nu \sim Pr^{1/8}$  for  $Pr \ll 1$  and  $Nu \sim Pr^0$  for  $Pr \gg 1$  at moderate  $Ra$ . Together, these datasets delineate the relevant parameter space for calibration.

From a strict standpoint, these scaling laws depend on the ranges of  $Ra$  and  $Pr$ , as well as on geometry, aspect ratio, wall roughness, and internal structure, and therefore cannot be represented by a single universal scaling law. Within the Reynolds-averaged framework, however, it is neither practical nor necessary to account for such dependencies explicitly. In engineering applications, where RANS models are primarily employed, the main objective is to reproduce the correct mean Nusselt number rather than the detailed flow organisation. As noted by Ahlers *et al.* (2009), parameters such as the aspect ratio and large-scale circulation exert only a weak influence on the mean  $Nu$ . Hence, the adopted scaling laws are considered sufficient for calibration over the practically relevant range  $10^{-3} \leq Pr \leq 10^3$  and  $Ra \leq 10^{10}$ .

The standard model exhibits its largest discrepancy from experiments in the  $Pr > O(1)$  regime, where the predicted  $Nu \sim Pr^{-0.4154}$  at fixed  $Ra$  contrasts with the nearly  $Pr$ -independent behaviour observed. For  $Pr < O(1)$ , the prediction  $Nu \sim Pr^{1/3}$  moderately departs from the experimental scaling  $Nu \sim Pr^{0.14}$  to  $Pr^{0.18}$  observed in experiments. In terms of  $Ra$  scaling, the observed  $Nu \sim Ra^{0.31}$  is marginally lower than the model prediction  $Nu \sim Ra^{1/3}$ , and the difference is small enough that no correction is applied. Overall, the standard model exaggerates the  $Pr$ -dependence, producing exponents of larger magnitude in both limits, which motivates the introduction of the present buoyant corrections.

#### 4.1. Definition of the correction parameters

The first step is to identify the parameters available for constructing the correction term. In the present formulation, the locally definable independent variables (Galilean invariants) reduce to six:

$$k, \quad \omega, \quad \nu, \quad a, \quad gb, \quad \frac{dT}{dz},$$

where  $g$  and  $b$  appear as a product because gravity acts only through buoyancy.

These six dimensional variables, expressed in terms of temperature, time, and length scales, can be reduced to three nondimensional parameters:

$$Re_T = \frac{\nu_T}{\nu}, \quad Pr, \quad \frac{\mathcal{P}_b}{\varepsilon}, \quad (4.1)$$

where  $Re_T$  is the turbulent Reynolds number (Wilcox 2006), and the final term represents the ratio of buoyant production to the dissipation rate of  $k$ , with  $\varepsilon = \beta^* k \omega$ .

In the near-wall region ( $z \leq \lambda_\nu$ ), the analytical distributions of  $Re_T$  and  $\mathcal{P}_b/\varepsilon$  are

$$Re_T = \left( \frac{z}{\lambda_\nu} \right)^{p+2}, \quad (4.2)$$

$$\frac{\mathcal{P}_b}{\varepsilon} = \left( \frac{z}{\lambda_\nu} \right)^{2-p} \frac{a_T/a}{1+a_T/a} = \frac{Pr}{Pr_T} \left( \frac{z}{\lambda_\nu} \right)^4 \left[ 1 + \frac{Pr}{Pr_T} \left( \frac{z}{\lambda_\nu} \right)^{p+2} \right]^{-1}, \quad (4.3)$$

with  $p = 3.307$ . For  $Pr > Pr_T$ ,  $\mathcal{P}_b/\varepsilon$  attains a maximum proportional to  $(Pr/Pr_T)^{(p-2)/(p+2)}$ , located at  $z < \lambda_\nu$ .

The turbulent Reynolds number  $Re_T$  reaches its maximum at  $z = L/2$ :

$$\begin{aligned} Re_T &= \frac{gbq}{\beta^* \nu} \left( \frac{L^2 \tau_c}{\nu} \right)^2 \\ &= \frac{1}{\beta^*} \left[ \frac{2}{\pi^2} \frac{\beta^*}{\sigma} (\beta_0 - \alpha \beta^* C_{\omega b}) \right]^{2/3} Ra^{1/3} Nu^{1/3} Pr^{-2/3}. \end{aligned} \quad (4.4)$$

Under the present one-dimensional configuration, the bulk value of  $\mathcal{P}_b/\varepsilon$  is nearly uniform and close to unity. In contrast, in two- or three-dimensional domains with convection cells,  $\varepsilon$  balances the total production  $(\mathcal{P} + \mathcal{P}_b)$ , so  $\mathcal{P}_b/\varepsilon$  need not remain unity.

In summary, any nondimensional correction function can be formulated in terms of the three parameters defined here, with its spatial variation inferred *a priori* from the present analytical framework.

#### 4.2. Correction of $Pr$ dependence

The standard model shows its largest discrepancy from experiments in the  $Nu$ – $Pr$  relation at fixed  $Ra$ , since the  $Pr$  dependence of buoyancy effects has not been explicitly addressed in previous formulations. This subsection corrects that dependence within the analytical framework established in §3.

Including the constants associated with buoyant thermal convection, the asymptotic form of Eq. (3.41) becomes

$$Nu \sim \begin{cases} Ra^{1/3} \left( Pr^{1/2} + C'_{\omega b}^{-1/2} Pr_T^{3/4} Pr^{-1/4} \right)^{-4/3}, & Pr \ll Pr_T \\ Ra^{1/3} \left( Pr_T^{0.1884} Pr^{0.3116} + C'_{\omega b}^{-1/2} Pr_T Pr^{-1/2} \right)^{-4/3}, & Pr \gg Pr_T. \end{cases} \quad (4.5)$$

Equation (4.5) indicates that the  $Pr$  dependence of  $Nu$  can be controlled through  $C'_{\omega b}$  and  $Pr_T$ . The terms  $C'_{\omega b}^{-1/2} Pr_T^{3/4} Pr^{-1/4}$  and  $Pr_T^{0.1884} Pr^{0.3116}$  dominate in the low- and high- $Pr$  limits, respectively, corresponding to the contributions of  $\Delta_{bulk}$  and  $\Delta_{BL}$  identified in §3.5. Accordingly, two complementary corrections are introduced: a bulk correction to  $C'_{\omega b}$  for  $Pr \ll 1$ , and a near-wall modification of  $a_T$  for  $Pr \gg 1$ .

Given that the uncorrected model predicts  $Nu \sim Pr^{1/3}$  in the low- $Pr$  regime, adopting a smaller asymptotic scaling exponent is effective for reproducing the observed behaviour  $Nu \sim Pr^{0.14}$  to  $Pr^{0.18}$  over  $0.001 \leq Pr \leq 1$ . Motivated by this consideration, the model targets the theoretical scaling  $Nu \sim Pr^{1/8}$  for  $Pr \ll 1$  proposed by Grossmann & Lohse (2000). To meet this target, the model must satisfy

$$\left( C'_{\omega b}^{-1/2} Pr_T^{3/4} Pr^{-1/4} \right)^{-4/3} \sim Pr^{1/8}, \quad (4.6)$$

then,

$$C'_{\omega b} \sim Pr^{-5/16} \quad \text{for } Pr \ll 1. \quad (4.7)$$

Here, the standard value  $Pr_T = 0.89$  is retained to avoid introducing unnecessary modifications to the model.

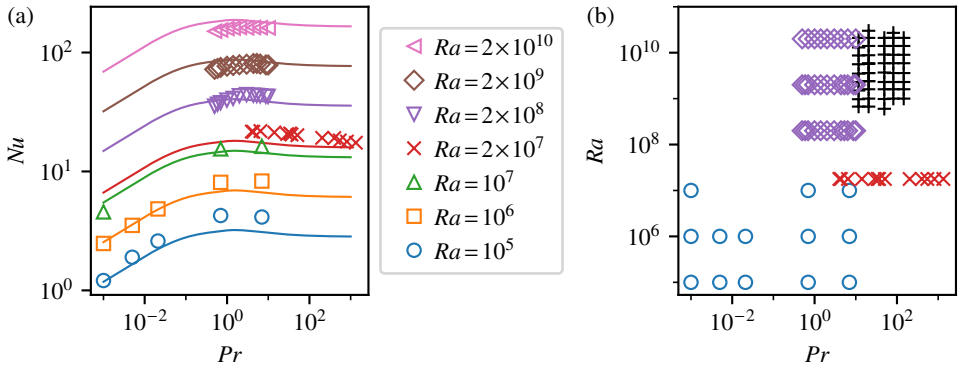


Figure 5. (a) Dependence of  $Nu$  on  $Pr$  using the applied corrections (Eqs. 4.8 and 4.10). The overlapping solid lines indicate the corrected analytical relations. (b) Reference data in the  $Ra$ - $Pr$  space: circles, crosses, diamonds, and pluses denote the datasets of Pandey *et al.* (2022), Xia *et al.* (2002), Stevens *et al.* (2011), and Li *et al.* (2021), respectively.

The correction to  $C'_{\omega b}$  is applied uniformly throughout the domain and is expressed as

$$C'_{\omega b} = c_1 + c_2 Pr^{-5/16}. \quad (4.8)$$

Here, the coefficients  $c_1$  and  $c_2$  determine both the Prandtl number at which the model enters the low- $Pr$  regime and the corresponding level of  $Nu$  in that regime.

To recover  $Nu \sim Pr^0$  for  $Pr \gg 1$ , so that  $\Delta_{BL}/\Delta \sim Pr^0$ , the near-wall integral term in Eq. (3.32) must satisfy

$$\int_0^1 \frac{1}{1 + a_T/a} dz' \sim \begin{cases} 1, & Pr \ll 1 \\ Pr^{-1/2}, & Pr \gg 1, \end{cases} \quad (4.9)$$

where  $z' = z/\lambda_\nu$ . The modelling objective is thus to design the near-wall  $a_T$  distribution so that this integral reproduces the target scaling. Following the approach in §3.4.1, the wall integral is approximated as

$$\int_0^1 \frac{1}{1 + a_T/a} dz' \approx \left(1 + d_1 Pr^{d_2/2}\right)^{-1/d_2}, \quad (4.10)$$

Analogously to  $c_1$  and  $c_2$ , the coefficients  $d_1$  and  $d_2$  determine both the Prandtl-number threshold for entering the high- $Pr$  regime and the corresponding magnitude of  $Nu$ .

The coefficients  $c_1$ ,  $c_2$ ,  $d_1$  and  $d_2$  are determined from reference data. Datasets are employed to span wide ranges of  $Ra$  and  $Pr$ :  $10^{-3} \leq Pr \leq 7$  and  $10^5 \leq Ra \leq 10^7$  from Pandey *et al.* (2022);  $4 \leq Pr \leq 1.3 \times 10^3$  at  $Ra = 1.78 \times 10^7$  from Xia *et al.* (2002);  $0.5 \leq Pr \leq 10$  and  $2 \times 10^8 \leq Ra \leq 2 \times 10^{10}$  from Stevens *et al.* (2011); and  $11.7 \leq Pr \leq 145.7$  and  $6 \times 10^8 \leq Ra \leq 3 \times 10^{10}$  from Li *et al.* (2021). The constants  $c_1$ ,  $c_2$ ,  $d_1$  and  $d_2$  are obtained by minimising the global least-squares error between the analytical  $Nu$  and the data using the differential-evolution algorithm (Storn & Price 1997), implemented as `scipy.optimize.differential_evolution` in Python (Gommers 2025). The optimal values are  $c_1 = 2.488$ ,  $c_2 = 0.2988$ ,  $d_1 = 1.125$  and  $d_2 = 1.173$ . Figure 5(a) demonstrates that the corrected analytical relation reproduces the observed  $Pr$  dependence across both low- and high- $Pr$  regimes. Figure 5(b) shows all employed data points in the  $Ra$ - $Pr$  space.

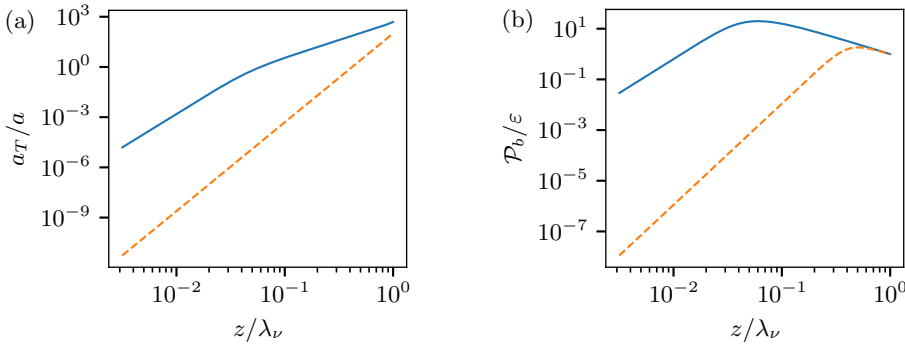


Figure 6. Analytical distributions at  $Pr = 10^2$ : (a) the turbulent thermal diffusivity and (b) the ratio of buoyant production to dissipation. Dashed and solid lines represent the original and corrected models, respectively.

To realise the target integral relation defined in Eq. (4.10), a near-wall correction function  $g$  is introduced to extend the conventional formulation  $a_T = v_T/Pr_T$ :

$$\frac{a_T}{a} = \frac{v_T}{Pr_T a} + g\left(Re_T, Pr, \frac{\mathcal{P}_b}{\epsilon}\right). \quad (4.11)$$

The dimensionless function  $g$  must satisfy the following conditions: (i)  $g = 0$  at the wall, because  $a_T$  must vanish at the wall. (ii)  $g = 0$  for  $\mathcal{P}_b/\epsilon = 0$ , ensuring that the correction leaves the standard formulation unchanged in the absence of buoyancy. (iii)  $g \ll v_T/(Pr_T a)$  for  $z \gg \lambda_\nu$ , indicating that the correction acts only as a near-wall modification. (iv)  $g \gg v_T/(Pr_T a)$  for  $z \leq \lambda_\nu$ , thereby enhancing the near-wall turbulent heat flux. This increase compensates for the underprediction of  $Nu$  at high  $Pr$  in the uncorrected model. In detail, the integral of the corrected  $a_T$  must satisfy Eq. (4.10) with  $d_1 = 1.125$  and  $d_2 = 1.173$ .

A convenient functional form satisfying these conditions is

$$g = e_0 Pr^{e_1} \left( \frac{\mathcal{P}_b}{\epsilon} \right)^{e_2} Re_T^{e_3}. \quad (4.12)$$

The corresponding near-wall distribution of  $a_T/a$  for  $z \leq \lambda_\nu$  becomes

$$\frac{a_T}{a} = \frac{Pr}{Pr_T} \left( \frac{z}{\lambda_\nu} \right)^{p+2} + e_0 Pr^{e_1} \left( \frac{z}{\lambda_\nu} \right)^{(2-p)e_2 + (p+2)e_3} \left( \frac{a_T/a}{1 + a_T/a} \right)^{e_2}. \quad (4.13)$$

The conditions on  $g$  imply (i)  $0 < e_3$ ; (ii)  $0 < e_2$  and  $0 < (2-p)e_2 + (p+2)e_3$ ; (iii)  $e_3 < 1$ ; and (iv)  $e_2 < 1$  and  $[(2-p)e_2 + (p+2)e_3]/(1-e_2) < p+2$ . For condition (iv), the quantity  $[(2-p)e_2 + (p+2)e_3]/(1-e_2)$  represents the exponent governing the near-wall power-law asymptotic scaling of  $a_T/a$  with respect to  $z$  as  $z \rightarrow 0$ , valid when  $e_2 < 1$ .

Values of  $e_2 = e_3 = 1/2$  are adopted to ensure sufficient numerical stability, as they lie near the middle of the inequality ranges and satisfy all the constraints. The remaining parameters  $e_0$  and  $e_1$  are optimised to reproduce the integral relation (4.10) for  $10^2 \leq Pr \leq 10^3$  using the same differential-evolution method, yielding  $e_0 = 7.141$  and  $e_1 = 0.8974$ .

As shown in figure 6(a), the correction increases  $a_T$  near the wall while leaving the bulk region almost unchanged. For  $e_2 = e_3 = 1/2$ , the asymptotic near-wall scaling (as  $z \rightarrow 0$ ) of  $a_T/a$  changes from  $z^{p+2} = z^{5.307}$  to  $z^4$ . The corresponding distribution of  $\mathcal{P}_b/\epsilon$ , shown in figure 6(b), changes from  $z^4$  to  $z^{6-p} = z^{2.693}$ . These modifications strengthen the

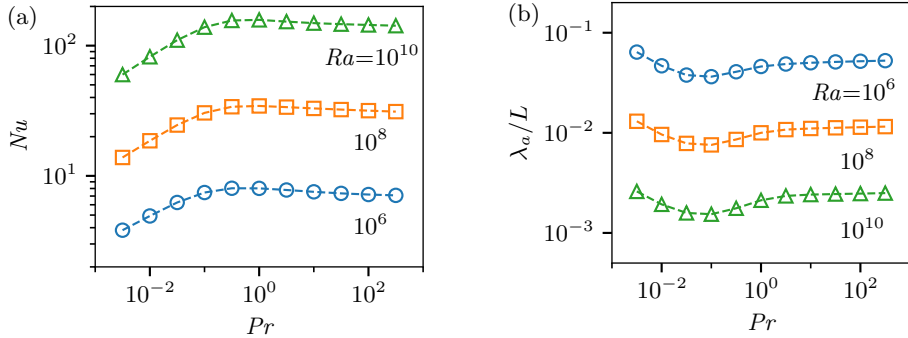


Figure 7. One-dimensional simulation results with  $Pr$ -correction: (a) the Nusselt number and (b) the thermal boundary-layer thickness as functions of  $Pr$ .

turbulent heat flux in the near-wall region, thereby compensating for the underprediction of  $Nu$  at high  $Pr$ . As a result, the corrected model increases  $Nu$  for  $Pr > 1$  while maintaining consistency with the standard framework.

In summary, the proposed corrections are

$$C_{\omega b} = -0.9752 - 0.2988 Pr^{-5/16} \quad \text{for } \mathcal{P}_b > 0, \quad (4.14)$$

$$\frac{a_T}{a} = \frac{Pr}{Pr_T} \frac{\nu_T}{\nu} + 7.141 Pr^{0.8974} \left[ \min \left( \max \left( \frac{\mathcal{P}_b}{\varepsilon}, 0 \right), C_{lim,b} \right) \right]^{1/2} \left( \frac{\nu_T}{\nu} \right)^{1/2}. \quad (4.15)$$

An upper limiter  $C_{lim,b}$  is introduced solely to ensure numerical robustness. During the early stages of a calculation, certain poorly scaled initial conditions (such as large  $k$  combined with very small  $\omega$ ) can lead to transiently large values of  $\mathcal{P}_b/\varepsilon$ . Such excursions amplify  $a_T$  locally, producing steep temperature gradients through the heat-balance relation, which then feed back into  $\mathcal{P}_b$  and may cause instabilities. To prevent this behaviour, the value is capped at  $C_{lim,b} = 100$ . This threshold is far above the converged values of  $\mathcal{P}_b/\varepsilon$  and therefore does not influence the final solution, while providing a safeguard against nonphysical transients during the convergence process.

Figure 7 presents the one-dimensional simulation results obtained with the  $Pr$  correction, using the same numerical method described in §3.6. As shown in figure 7(a), the corrected  $a_T$  (Eq. 4.15) successfully reproduces the  $Nu \sim Pr^0$  scaling for  $Pr > 1$ . For  $Ra = 10^6$ , the simulations yield  $Nu = 13.1 Pr^{0.213}$  over  $10^{-2.5} \leq Pr \leq 10^{-1.5}$ , consistent with the reference data of Pandey *et al.* (2022), which reported  $Nu = 11.3 Pr^{0.220}$  for  $0.001 \leq Pr \leq 0.021$ . These results indicate that the correction to  $C_{\omega b}$  effectively reproduces the  $Nu$  dependence in the low- $Pr$  regime. As illustrated in figure 7(b), the correction also improves the prediction of the thermal boundary-layer thickness. The DNS of Stevens *et al.* (2011) show that the thermal boundary-layer thickness remains nearly independent of  $Pr$  for  $Pr > 1$ . The corrected model accurately reproduces this behaviour, whereas the uncorrected model erroneously predicts  $\lambda_a/L \sim Pr^{0.4041}$  (see figure 3b). Overall, the proposed buoyancy correction substantially enhances the predictive performance of the standard  $k-\omega$  model while preserving internal consistency and numerical robustness.

#### 4.3. $C_{\omega b}$ for stable stratification

After calibrating  $C_{\omega b}$  for unstable stratification ( $\mathcal{P}_b > 0$ ), the analysis is extended to the stably stratified regime ( $\mathcal{P}_b < 0$ ) to complete the formulation of the  $\omega$  equation. As summarised in §2.2, Rodi (1987) recommended setting  $C_{\varepsilon b} = 0$  for  $\mathcal{P}_b < 0$ , an approach

that has been widely adopted. Through the correspondence between the  $k$ - $\varepsilon$  and  $k$ - $\omega$  formulations (Eq. 2.18), this prescription corresponds to  $C_{\omega b} \approx -2$ . As an alternative to empirical calibration, the present study examines an analytical procedure for determining  $C_{\omega b}$  for  $\mathcal{P}_b < 0$ .

This analytical approach is guided by the canonical case of homogeneous stably stratified shear flow, which provides a well-defined stability threshold for model consistency. As discussed in §1, models for  $\mathcal{P}_b < 0$  are typically constrained by the behaviour of stably stratified shear flows, where linear stability analyses predict flow stabilization once the flux Richardson number  $Ri_f = -\mathcal{P}_b/\mathcal{P}$  exceeds approximately 0.25 (Gibson & Launder 1978; Durbin & Pettersson-Reif 2011). Following this benchmark, Burchard & Baumert (1995); Burchard (2007) analysed the  $k$ - $\varepsilon$  model from a dynamical-systems perspective to determine the appropriate form of  $C_{\varepsilon b}$  for stably stratified shear flows. This framework treats the  $k$ - $\varepsilon$  model as a set of ordinary differential equations for  $k(t)$  and  $\varepsilon(t)$ , whose trajectories in the  $(k, \varepsilon)$  phase space are analysed to determine the stabilization conditions. For further discussions on dynamical-systems analyses of RANS models, see Pettersson Reif *et al.* (2006); Rumsey *et al.* (2006); Rumsey (2007).

In the same framework, the appropriate  $C_{\omega b}$  for  $\mathcal{P}_b < 0$  can be determined analytically. The idealized configuration corresponds to a homogeneous stably stratified shear flow in which  $k$  and  $\omega$  vary only with time. Under these conditions, the production terms become

$$\mathcal{P} = \nu_T S^2 = S^2 \frac{k}{\omega}, \quad \mathcal{P}_b = -g\beta \frac{\nu_T}{Pr_T} \frac{dT}{dz} = -\left( \frac{g\beta}{Pr_T} \frac{dT}{dz} \right) \frac{k}{\omega} = -Ri_f \mathcal{P},$$

where  $S^2 = S_{ij}S_{ij}$  and  $dT/dz > 0$ , so that  $\mathcal{P} > 0$  and  $\mathcal{P}_b < 0$  with constant  $S$  and  $Ri_f > 0$ .

Under this configuration, the  $k$ - $\omega$  equations reduce to

$$\frac{dk}{dt} = k \left[ \frac{(1 - Ri_f)S^2}{\omega} - \beta^* \omega \right], \quad (4.16)$$

$$\frac{d\omega}{dt} = \alpha S^2 (1 - Ri_f C_{\omega b}) - \beta_0 \omega^2. \quad (4.17)$$

Because  $\omega$  evolves independently of  $k$ , its temporal behaviour is examined first. By definition,  $\omega(t)$  must remain positive for any  $Ri_f$ , implying that the source term must stay non-negative even in the limit of large  $Ri_f$ . This constraint implies

$$C_{\omega b} \leq 0 \quad \text{for } \mathcal{P}_b < 0, \quad (4.18)$$

as a positive  $C_{\omega b}$  would drive  $d\omega/dt < 0$  near  $\omega \rightarrow 0$ , yielding unphysical negative values of  $\omega$ .

For  $C_{\omega b} \leq 0$ ,  $\omega$  asymptotically approaches a steady state ( $t \rightarrow \infty$ ) given by

$$\omega_\infty = \left[ \frac{\alpha S^2}{\beta_0} (1 - Ri_f C_{\omega b}) \right]^{1/2}, \quad (4.19)$$

which is readily seen to be a stable equilibrium, as  $d\omega/dt < 0$  for  $\omega > \omega_\infty$  and  $d\omega/dt > 0$  for  $\omega < \omega_\infty$ .

Substituting  $\omega_\infty$  into the  $k$  equation gives

$$\frac{dk}{dt} = k \left[ \frac{(1 - Ri_f)S^2}{\omega_\infty} - \beta^* \omega_\infty \right]. \quad (4.20)$$

For the turbulent kinetic energy to decay with time, the right-hand side must be negative:

$$\frac{(1 - Ri_f)S^2}{\omega_\infty} - \beta^* \omega_\infty < 0.$$

Rearranging yields the stability condition

$$Ri_f > \left(1 - \frac{\alpha\beta^*}{\beta_0}\right) \left(1 - \frac{\alpha\beta^*}{\beta_0} C_{\omega b}\right)^{-1}. \quad (4.21)$$

Hence, the value of  $C_{\omega b}$  that reproduces the conventional stabilization threshold of  $Ri_f \geq 0.25$  is

$$C_{\omega b} = \frac{\beta_0}{\alpha\beta^*} - \frac{1}{0.25} \left( \frac{\beta_0}{\alpha\beta^*} - 1 \right) = -0.5385 \quad \text{for } \mathcal{P}_b < 0. \quad (4.22)$$

By comparison, the earlier empirical recommendation  $C_{\omega b} \approx -2$  would predict stabilization at  $Ri_f \geq 0.146$ , lower than the theoretical benchmark.

Combining Eqs. (4.14) and (4.22) gives the complete  $\omega$  equation:

$$\begin{aligned} \frac{\partial \omega}{\partial t} + U_j \frac{\partial \omega}{\partial x_j} &= \alpha \frac{\omega}{k} [\mathcal{P} + C_{\omega b}^+ \max(\mathcal{P}_b, 0) + C_{\omega b}^- \min(\mathcal{P}_b, 0)] \\ &\quad - \beta_0 f_\beta \omega^2 + \frac{\sigma_d}{\omega} \frac{\partial k}{\partial x_j} \frac{\partial \omega}{\partial x_j} + \frac{\partial}{\partial x_j} \left[ \left( \nu + \sigma \frac{k}{\omega} \right) \frac{\partial \omega}{\partial x_j} \right], \end{aligned} \quad (4.23)$$

where the buoyancy coefficients are

$$C_{\omega b}^+ = -0.9752 - 0.2988 Pr^{-5/16}, \quad C_{\omega b}^- = -0.5385. \quad (4.24)$$

As a further quantitative validation, a stably stratified turbulent plane channel flow is considered. The upper hot wall ( $T = \Delta$  at  $z = h$ ) and the lower cold wall ( $T = 0$  at  $z = -h$ ) are both isothermal and no-slip. Gravity acts in the vertically downward ( $-z$ ) direction, while the flow is driven horizontally. The dimensionless control parameters are the friction Reynolds number,  $Re_\tau = U_\tau h / \nu$ , where  $U_\tau (= \sqrt{\nu dU/dz}$  at the walls) is the friction velocity and  $h$  is the channel half-height, and the friction Richardson number,  $Ri_\tau = g b \Delta h / U_\tau^2$ . The dimensionless output quantities are the Nusselt number,  $Nu = 2hq / (a\Delta)$ , and the bulk Reynolds number,  $Re_b = U_b h / \nu$ , where  $U_b$  is the bulk mean velocity.

The choices  $C_{\omega b} = -0.5385$  and  $C_{\omega b} = -2$  are tested under the same conditions as the DNS of Garcia-Villalba & del Álamo (2011). As a baseline, the case without buoyancy ( $Ri_\tau = 0$ ) is first examined using the standard  $k-\omega$  model: (i) for  $Re_\tau = 180$ , DNS yields  $Re_b = 2.82 \times 10^3$  and  $Nu = 6.03$ , while RANS yields  $Re_b = 2.75 \times 10^3$  and  $Nu = 6.36$ ; (ii) for  $Re_\tau = 550$ , DNS yields  $Re_b = 1.01 \times 10^4$  and  $Nu = 16.44$ , while RANS yields  $Re_b = 1.03 \times 10^4$  and  $Nu = 17.0$ . Here,  $Pr = 0.7$ . Thus, for this reference case, the standard model predicts the mean heat transport within approximately 6% relative error.

Figure 8 shows the model predictions as a function of  $Ri_\tau$  at fixed (a)  $Re_\tau = 180$  and (b)  $Re_\tau = 550$ . When  $C_{\omega b} = -0.5385$  is used, the model predicts larger  $Nu$  and smaller  $Re_b$  relative to  $C_{\omega b} = -2$ : this occurs because the source term in the  $\omega$  equation becomes smaller, leading to smaller  $\omega$  and therefore larger  $\nu_T = k/\omega$ . Within the present parameter range,  $C_{\omega b} = -2$  generally yields better agreement, but the trends indicate that the predictions for  $C_{\omega b} = -0.5385$  become closer to DNS at higher  $Re_\tau$ . For  $Re_\tau = 550$ , the  $Nu$  prediction using  $C_{\omega b} = -0.5385$  shows a slight improvement. Overall, the differences in the dimensionless mean quantities associated with the two constants remain within about 20%.

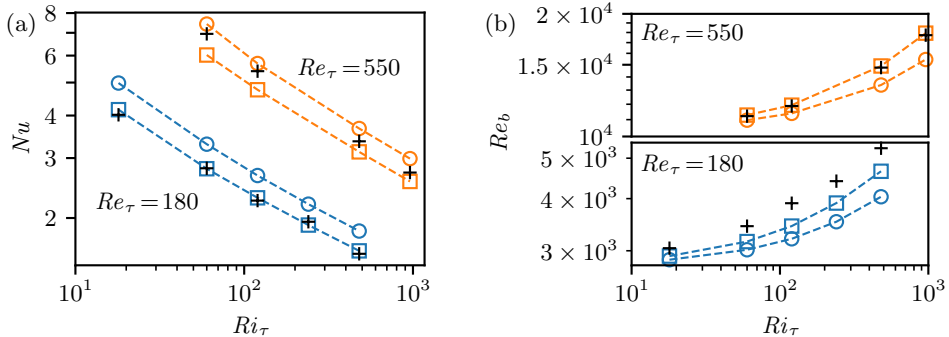


Figure 8. Stably stratified channel flow at  $Pr = 0.7$ . (a) Nusselt number and (b) bulk Reynolds number as functions of the friction Richardson number, at fixed friction Reynolds numbers of 180 (upper curves) and 550 (lower curves). Circles and squares denote the simulation results for  $C_{\omega b} = -0.5385$  and  $C_{\omega b} = -2$ , respectively. Crosses denote the DNS data of Garcia-Villalba & del Álamo (2011).

In summary, while the analytically derived value  $C_{\omega b} = -0.5385$  produces a stability threshold that is internally consistent, the quantitative accuracy of both  $C_{\omega b} = -2$  and  $C_{\omega b} = -0.5385$  is configuration- and parameter-dependent. Even in a purely Reynolds-averaged sense, buoyancy damping affects only the gravity-aligned component of  $k$ , which induces strong anisotropy in the Reynolds stresses — a feature that is not naturally accommodated within the Boussinesq eddy-viscosity closure of the standard model. Higher-order treatments at the level of Reynolds-stress and heat-flux closures can be found in Lazeroms *et al.* (2013), but a more comprehensive treatment of such issues lies beyond the present scope, which is limited to optimising the model within the standard  $k$ - $\omega$  formulation.

## 5. Model evaluation

This section assesses the performance of the buoyancy-corrected  $k$ - $\omega$  model across a range of buoyancy-driven flows, extending beyond the one-dimensional Rayleigh–Bénard configuration. The corrected formulation preserves the structure of the standard model and differs only through the buoyancy-related modifications introduced in Eqs. (4.15, 4.23, 4.24). For evaluating the uncorrected standard model, the conventional choices  $C_{\omega b} = 1$  for  $\mathcal{P}_b > 0$  and  $C_{\omega b} = -2$  for  $\mathcal{P}_b < 0$  are adopted.

Previous RANS studies of buoyancy-driven turbulence have largely focused on a limited set of canonical configurations. Vertically heated natural convection in enclosed cavities has been the most widely explored, typically within the ranges  $Pr = 0.7–7$  and  $10^8 \leq Ra \leq 10^{15}$  (Ince & Launder 1989; Henkes *et al.* 1991; Peng & Davidson 1999; Dol & Hanjalić 2001; Kenjereš *et al.* 2005; Dehoux *et al.* 2017). Rayleigh–Bénard convection has also been examined, although generally for  $Ra \leq 10^9$  at fixed  $Pr = 0.7$  (Kenjereš & Hanjalić 1995; Choi & Kim 2012). Vertical natural convection in channels has received comparatively less attention and is usually restricted to  $Ra = 10^5–10^7$  at  $Pr = 0.7$  (Dol *et al.* 1999; Dehoux *et al.* 2017).

Despite spanning several orders of magnitude in Rayleigh number, these investigations cover only a small number of geometries and share common limitations. Systematic evaluation of Prandtl-number effects is rare, and many buoyancy-correction approaches rely on ad hoc functional forms whose validity has been demonstrated only within restricted flow regimes. As a result, the broader applicability of these corrections remains uncertain.

The present study examines a wider variety of buoyancy-driven flows: (i) two internally heated convection configurations; (ii) unstably stratified Couette flow (mixed convection); (iii) Rayleigh–Bénard convection in a two-dimensional square cavity; and (iv) vertically heated natural convection in two-dimensional rectangular cavities with aspect ratios of 1 and 4.

Vertical channel flow is not included. Although buoyancy formally drives the flow in this configuration, the imposed temperature gradient is strictly perpendicular to gravity. Under the gradient-diffusion hypothesis used for turbulent heat-flux modelling, this alignment yields  $\mathcal{P}_b = 0$  throughout the domain, and the buoyancy-correction terms introduced here therefore have no effect.

### 5.1. Internally heated convection

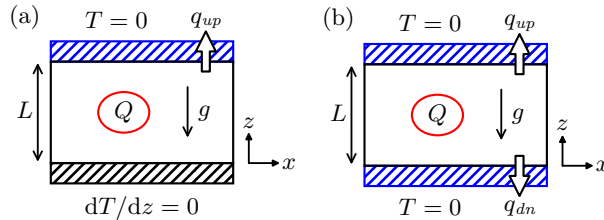


Figure 9. Internally heated convection setup for (a) top cooling and (b) top-and-bottom cooling condition.

Internally heated convection is used here to assess whether the correction derived for Rayleigh–Bénard convection also applies to buoyancy-driven flows whose temperature distributions differ fundamentally from the Rayleigh–Bénard configuration. A spatially uniform volumetric heat source  $Q$  (defined in Eq. 2.2) is imposed throughout the one-dimensional domain. Two configurations are considered, as illustrated in Figure 9:

(a) Top cooling: the upper wall is isothermal and cooled, while the lower wall is adiabatic; that is,  $T = 0$  at  $z = L$  and  $dT/dz = 0$  at  $z = 0$ . In this case, the upward heat flux  $q_{up}$  ( $= -adT/dz$  at  $z = L$ ) satisfies  $q_{up} = QL$ .

(b) Top-and-bottom cooling: both the upper and lower walls are isothermal at the same temperature, such that  $T = 0$  at  $z = 0$  and  $z = L$ . The upward and downward conductive heat fluxes ( $q_{up}$  and  $q_{dn}$ ) satisfy the global balance  $QL = q_{up} + q_{dn}$ .

For both configurations, the top and bottom walls satisfy no-slip boundary conditions. To characterise the flow, the modified Rayleigh number is defined as  $Ra' = gbQL^5/(va^2)$ . The dimensionless temperature is  $T^* = aT/(L^2Q)$ , and either the domain-averaged temperature  $T_{avg}^*$  or the maximum temperature  $T_{max}^*$  is used for comparison against reference data. For the top-and-bottom cooling configuration (Figure 9(b)), an additional output parameter is introduced — the fraction of the total generated heat escaping through the lower wall,  $F_{dn} = q_{dn}/(QL)$ .

First, Figure 10(a) presents the maximum dimensionless temperature for the top-cooling configuration at  $Pr = 6$ . The experimental correlation of Kulacki & Emara (1977) is  $T_{max}^* = 2.96(Ra')^{-0.227}$  for  $2.75 \leq Pr \leq 6.86$  and  $10^3 \leq Ra' \leq 10^{12}$ . The standard  $k-\omega$  model with  $C_{\omega b} = 1$  yields  $T_{max}^* = 0.520(Ra')^{-0.288}$  for  $10^7 \leq Ra' \leq 10^{10}$ , whereas the corrected  $k-\omega$  model yields  $T_{max}^* = 0.325(Ra')^{-0.245}$ .

The modelled scaling behaviour of  $T_{max}^*$  in internally heated convection can be interpreted in relation to Rayleigh–Bénard convection through dimensional analysis. Because  $T_{max}^*$  represents temperature normalised by a characteristic heat-flux scale, it scales as  $T_{max}^* \sim Nu^{-1}$ . In addition, if the Rayleigh number is estimated as  $Ra \sim gbT_{max}^*L^3/(va)$ , then

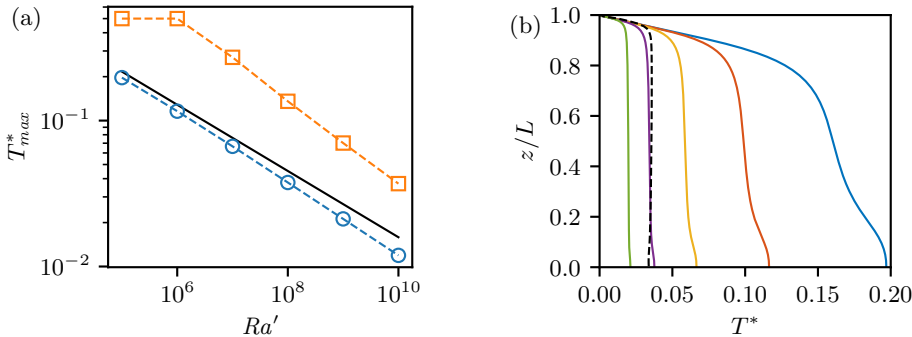


Figure 10. Internally heated convection with top cooling at  $Pr = 6$ . (a) Maximum dimensionless temperature as a function of the internal Rayleigh number. The solid line is the experimental correlation of Kulacki & Emara (1977); circles are the corrected  $k-\omega$  model; squares are the standard  $k-\omega$  model with  $C_{\omega b} = 1$ . (b) Dimensionless temperature profiles. The solid lines correspond to the corrected  $k-\omega$  model at  $Ra' = 10^5, 10^6, 10^7, 10^8$  and  $10^9$ , ordered from right to left. The dashed line shows the DNS results of Nourgaliev & Dinh (1997) at  $Ra = 1.86 \times 10^8$ .

$Ra \sim T_{max}^* Ra'$  follows. Substituting these relations into the Rayleigh–Bénard model scaling  $Nu \sim Ra^{1/3}$  yields  $T_{max}^* \sim (Ra')^{-1/4}$ .

The key conclusion of this test is that the model constants optimised for Rayleigh–Bénard convection yield markedly improved predictions even for the qualitatively different problem of internally heated convection. The widely used choice  $C_{\omega b} = 1$  strongly underpredicts  $Nu$  in Rayleigh–Bénard convection and correspondingly overpredicts  $T_{max}^*$  in internally heated convection. In contrast, the model corrected on the basis of Rayleigh–Bénard scaling produces substantially improved agreement.

Figure 10(b) shows the temperature profiles as a function of  $Ra'$ . The DNS results of Nourgaliev & Dinh (1997) at  $Ra = 1.86 \times 10^8$  exhibit an almost uniform temperature in the bulk region, except near the cooled upper wall. The  $k-\omega$  model reproduces this behaviour accurately.

Next, figure 11 presents the results for the top-and-bottom cooling configuration. The parameter ranges are chosen to enable direct comparison with the DNS results of Goluskin & van der Poel (2016). This case contains regions with  $\mathcal{P}_b < 0$  owing to cooling at the lower boundary. For this configuration, the proposed correction again yields substantially improved prediction accuracy for both the dimensionless average temperature  $T_{avg}^*$  (figure 11(a,c)) and the downward heat flux fraction  $F_{dn}$  (figure 11(b,d)), with particularly notable improvement in the predicted dependence on  $Pr$ .

The accuracy of  $F_{dn}$  depends on how the model represents stably stratified regions. As shown in figures 11(b,d), the analytically derived value  $C_{\omega b} = -0.5385$  (§4.3) yields predictions that are noticeably more consistent than those obtained using the conventional choice  $C_{\omega b} = -2$ . The difference arises from how strongly each coefficient damps  $k$  under stable stratification. In figure 11(b), the variation of  $F_{dn}$  with increasing  $Ra'$  for a given  $C_{\omega b}$  is consistent with the mechanism described in §4.3: using  $C_{\omega b} = -2$  suppresses  $k$  more strongly than  $C_{\omega b} = -0.5385$ , thereby reducing the turbulent heat transport. A similar behaviour occurs near the lower stably stratified region. Because the uncorrected model employs  $C_{\omega b} = -2$ , the excessive damping of  $k$  in the stable region reduces the turbulent heat transport more rapidly, leading to a steeper decline in  $F_{dn}$  as  $Ra'$  increases.

Figure 11(c) shows that, at fixed  $Ra' = 2 \times 10^7$ , the DNS results yield approximately constant  $T_{avg}^*$  for  $0.1 \leq Pr \leq 1$ . In contrast, the uncorrected model produces a rapid increase of  $T_{avg}^*$  with increasing  $Pr$ . This behaviour is consistent with the fact that  $T_{avg}^*$  corresponds

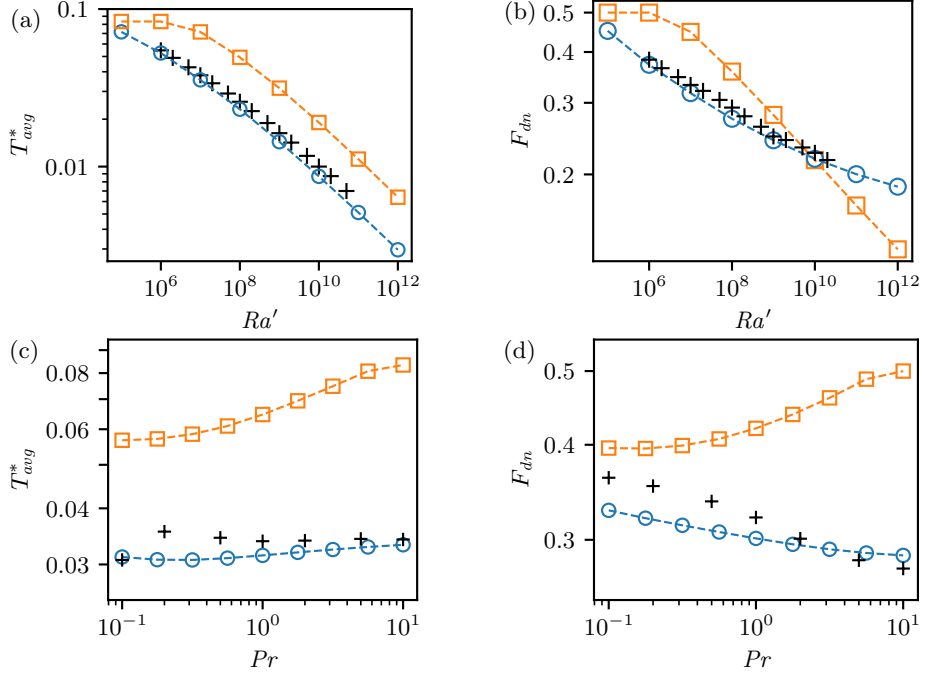


Figure 11. Internally heated convection with top-and-bottom cooling. Circles denote the corrected  $k-\omega$  model; squares denote the standard  $k-\omega$  model; crosses denote the DNS results of Goluskin & van der Poel (2016). Panels (a) and (c) show the dimensionless average temperature, and panels (b) and (d) show the fraction of heat escaping across the bottom boundary.  $Pr = 1$  is used in (a) and (b) to illustrate the dependence on  $Ra'$ , whereas  $Ra' = 2 \times 10^7$  is used in (c) and (d) to illustrate the dependence on  $Pr$ .

to  $Nu^{-1}$ , and that the uncorrected model tends to underpredict  $Nu$  at large  $Pr$  in Rayleigh–Bénard convection. The correction derived from Rayleigh–Bénard convection removes this deficiency, producing a substantially more accurate Prandtl-number dependence for  $T_{avg}^*$ .

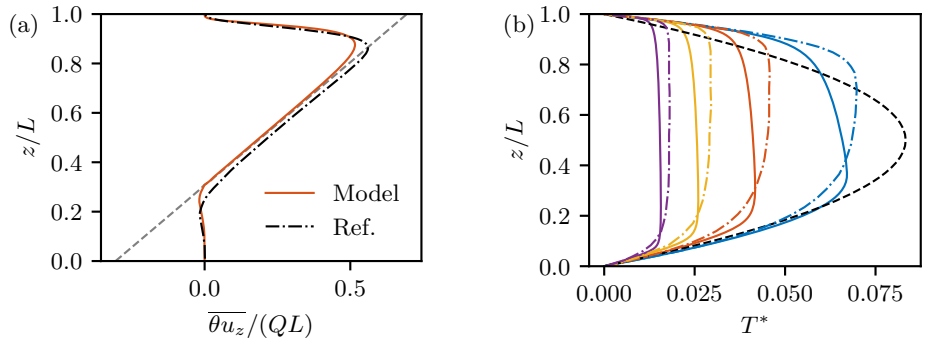


Figure 12. Simulation results for internally heated convection with top-and-bottom cooling using the corrected  $k-\omega$  model. (a) Turbulent heat-flux distribution at  $Ra' = 10^7$  and  $Pr = 7$  from the corrected  $k-\omega$  model (solid line) and the DNS results of Wörner *et al.* (1997) (dash-dotted line). The dashed line indicates the total heat flux predicted by the model. (b) Dimensionless temperature distribution from the corrected  $k-\omega$  model (solid lines) and the DNS results of Goluskin & van der Poel (2016) (dash-dotted lines). For fixed  $Pr = 1$ , each line corresponds to  $Ra' = 10^6, 10^7, 10^8$ , and  $10^9$ , ordered from right to left. The dashed line indicates the pure-conduction state.

Figure 12 presents the temperature and heat-transport distributions for internally heated convection with top-and-bottom cooling. Figure 12(a) shows that the corrected  $k-\omega$  model reproduces the turbulent heat-flux distribution of the DNS of Wörner *et al.* (1997) with good fidelity. In contrast, the temperature profiles in Figure 12(b) exhibit clear discrepancies between the model and the DNS. The DNS shows an increase of temperature toward the upper boundary, whereas the RANS solution predicts a decrease in temperature in the upper region of the domain. This discrepancy stems from a basic consequence of the closure formulation. In this configuration, the local heat-flux direction is downward near the cooled lower wall, but upward throughout most of the remaining domain. Within the gradient-diffusion framework underlying  $k-\omega$  standard closures, a positive turbulent heat flux  $\theta\bar{u}_z > 0$  in the region where  $\mathcal{P}_b > 0$  necessarily implies that temperature must decrease with height. Consequently, the DNS behaviour in the upper region cannot be captured by this class of closures. Despite this unavoidable inconsistency, the corrected model accurately predicts the heat-flux distribution, the mean temperature, and the partitioning of heat leaving the upper and lower boundaries. This outcome indicates that the present correction remains sufficiently effective for engineering purposes.

## 5.2. Unstably stratified Couette flow

To assess the model's applicability beyond purely buoyancy-driven conditions, it is necessary to examine a configuration in which shear and buoyancy interact. The unstably stratified Couette flow investigated by Blass *et al.* (2020, 2021) provides a suitable test case, representing a mixed-convection regime in which both mechanisms contribute to heat and momentum transport.

In this configuration, gravity acts in the downward ( $-z$ ) direction and the flow is periodic in the horizontal ( $x$ ) direction. The boundary conditions are  $U_x = -U_w$  and  $T = \Delta$  at  $z = 0$ , and  $U_x = U_w$  and  $T = 0$  at  $z = L$ . The Rayleigh and Nusselt numbers follow the definitions used for Rayleigh–Bénard convection. The wall-shear Reynolds number,  $Re_w = U_w L / \nu$ , serves as the control parameter, while the friction Reynolds number,  $Re_\tau = U_\tau L / \nu$ , is treated as an output quantity.

Figure 13 compares the predictions of the corrected model with DNS results (Yerragolam *et al.* 2022; Blass *et al.* 2020, 2021). Panels (a,b) show the dependence on  $Re_w$  at  $Pr = 1$ , covering a wide range of Rayleigh and Reynolds numbers. Across all tested conditions, within  $Ra \leq 10^8$  and  $Re_w \leq 10^4$ , the corrected model reproduces both the Nusselt number and the friction Reynolds number with high accuracy.

This behaviour can be understood by considering the limiting regimes. For  $Ra = 0$ , the standard  $k-\omega$  model predicts the trends of  $Nu$  and  $Re_\tau$  in passive-scalar Couette flow with errors typically below 10%. Likewise, in the absence of shear, the present model reproduces the mean Nusselt number of Rayleigh–Bénard convection to within a similar accuracy. DNS results for the mixed regime indicate a smooth transition between these two limits, with no evidence of strong nonlinear interactions between shear and buoyancy for the parameter range considered. Consequently, the intermediate behaviour is comparatively well captured by the RANS closure.

Panels (c,d) examine the dependence on the Prandtl number by fixing  $Re_w = 4000$  and  $Ra = 10^6$  and varying  $0.22 \leq Pr \leq 4.6$ . In figure 13(c), the corrected model predicts the mean Nusselt number to within approximately 10% of DNS. In figure 13(d), the model consistently underpredicts  $Re_\tau$  by approximately 5–8%. As indicated in the figure, even in the absence of buoyancy, the standard model intrinsically underpredicts  $Re_\tau$  by about 6% under comparable conditions. This baseline discrepancy therefore appears to carry

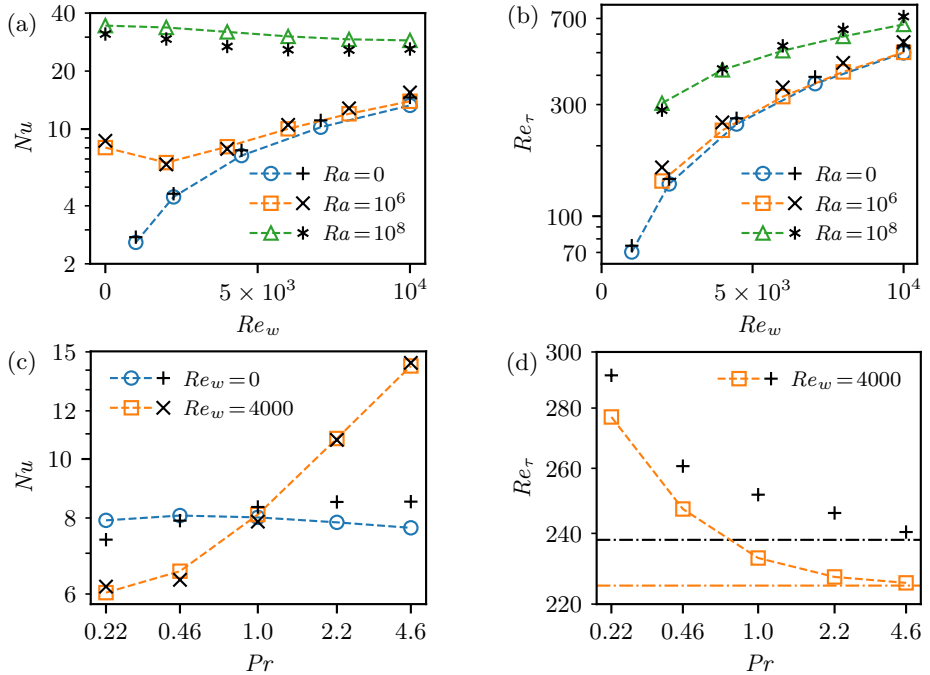


Figure 13. Unstably stratified Couette flow simulation results of the corrected  $k$ - $\omega$  model. Panels (a,c) show the Nusselt number, and panels (b,d) show the friction Reynolds number, each plotted against one of the two governing parameters: (a,b) variation with the wall-shear Reynolds number at  $Pr = 1$ , and (c,d) variation with the Prandtl number at  $Ra = 10^6$ . Circle, square, and triangle markers denote predictions from the corrected  $k$ - $\omega$  RANS model. Crosses, plus signs, and asterisks denote DNS data: Yerragolam *et al.* (2022) for the  $Ra = 0$  cases in (a,b); Blass *et al.* (2020) for the remaining cases in (a,b); and Blass *et al.* (2021) for the data in (c,d). The dash-dot horizontal lines in (d) mark the  $Re_\tau$  values at  $Re_w = 4000$  and  $Ra = 0$ , with the upper line corresponding to the DNS result (Blass *et al.* 2020) and the lower to the  $k$ - $\omega$  model.

over and yield the overall underprediction in  $Re_\tau$ . Nevertheless, the proposed buoyancy correction reproduces the increase of  $Re_\tau$  with decreasing  $Pr$  with high accuracy.

Taken together, these results show that the proposed correction integrates smoothly into the standard  $k$ - $\omega$  framework and remains robust in a mixed-convection environment where shear and buoyancy interact.

### 5.3. Rayleigh–Bénard convection in a two-dimensional square cavity

To evaluate the robustness of the Prandtl-number correction beyond the one-dimensional setting, the model is further assessed in two-dimensional Rayleigh–Bénard convection within a square cavity. The vertical walls, which are parallel to gravity, are adiabatic, and all boundaries satisfy no-slip conditions.

Figure 14 shows the mean Nusselt number predicted by the two-dimensional simulations across a range of Rayleigh and Prandtl numbers. Owing to the presence of large-scale circulation in two dimensions, the heat transfer departs from the one-dimensional result, but the deviation remains moderate. For example, the difference between the one- and two-dimensional predictions is within approximately 10% at  $Ra = 2 \times 10^8$ . These trends indicate that the Prandtl-number correction formulated under one-dimensional assumptions (§4) retains sufficient accuracy in two dimensions and is capable of reproducing the DNS scaling behaviour within the tested parameter space.

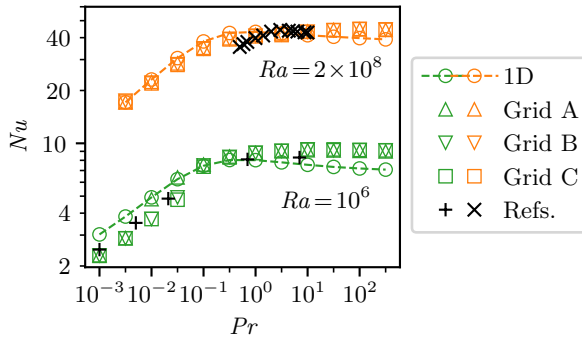


Figure 14. Rayleigh–Bénard convection simulation results of the corrected  $k$ – $\omega$  model. Two-dimensional simulations in a square domain are performed using three grid resolutions—Grid A ( $60^2$ ), Grid B ( $100^2$ ), and Grid C ( $150^2$ )—and compared with the corresponding one-dimensional (1D) simulation. DNS reference data are taken from Pandey *et al.* (2022) (plus signs) and Stevens *et al.* (2011) (crosses).

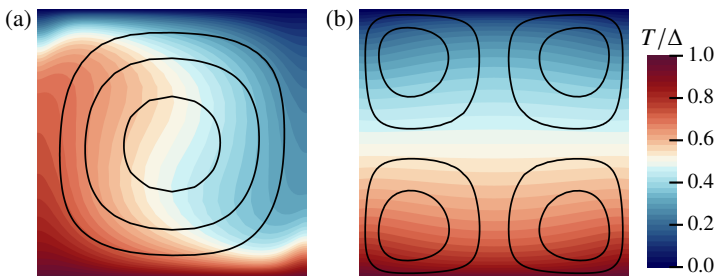


Figure 15. Simulation results from the corrected  $k$ – $\omega$  model. For identical control parameters,  $Ra = 10^6$  and  $Pr = 10^{-2}$ , two distinct converged states are obtained: (a) a single convection cell and (b) four convection cells. Black solid lines denote streamfunction contours.

Grid independence for the two-dimensional cases is examined using three meshes constructed with identical geometric growth ratios in both coordinate directions and symmetric about the domain mid-plane. Grid A employs  $60^2$  cells with a growth ratio of 1.20 and a minimum spacing of  $1.26 \times 10^{-3}$  (normalised by the domain length) near the walls; Grid B employs  $100^2$  cells with a growth ratio of 1.14 and a minimum spacing of  $1.19 \times 10^{-4}$ ; Grid C employs  $150^2$  cells with a growth ratio of 1.10 and a minimum spacing of  $4.46 \times 10^{-5}$ . Steady solutions are obtained by neglecting the temporal derivatives and iterating until convergence.

For most Rayleigh–Prandtl combinations, the predicted Nusselt number is effectively grid-independent. However, at  $Ra = 10^6$  and  $Pr = 10^{-1.5}$  or  $10^{-2}$ , discrepancies of up to 20% arise among the three meshes. Further investigation reveals that this sensitivity originates not from numerical resolution, but from the existence of multiple converged states: even on the same mesh, different initial conditions lead to distinct large-scale circulation patterns.

Figure 15 illustrates the two representative steady states observed at  $Pr = 10^{-2}$  and  $Ra = 10^6$ . Depending on the initial condition, the solution may converge either to a single-cell circulation with  $Nu = 4.81$ , or to a four-cell configuration with  $Nu = 3.71$ . In the latter case, interactions among adjacent circulation rolls reduce the overall flow intensity, resulting in a lower heat-transfer rate compared with the single-cell state. If the large-scale circulation pattern is the same, the predicted Nusselt number is approximately

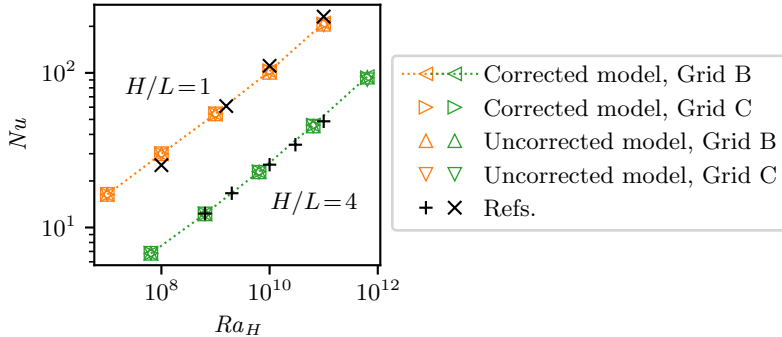


Figure 16. Natural convection in a rectangular cavity with differentially heated vertical walls. The overall Nusselt number is shown as a function of the height-based Rayleigh number at  $Pr = 0.71$ . The upper and lower dotted curves (with adjacent markers) correspond to aspect ratios  $H/L = 1$  and  $H/L = 4$ . Four simulation cases are presented using the corrected and uncorrected models on two grids — Grid B ( $100^2$ ) and Grid C ( $150^2$ ). Plus signs and crosses denote DNS data from Trias *et al.* (2007, 2010) and Sebilleau *et al.* (2018), respectively.

grid-independent across the three meshes. In contrast, at higher  $Ra$  or  $Pr$ , such pronounced changes in the predicted heat flux due to different convection-cell patterns are not observed.

In summary, the presence of large-scale circulation in two dimensions introduces moderate deviations from the one-dimensional predictions. However, these effects are typically limited to within 20%, and the corrected model maintains its ability to reproduce the proper global  $Nu$ – $Ra$ – $Pr$  trends. Taken together, these results suggest that the Prandtl-number correction can retain its robustness beyond the one-dimensional setting, supporting its applicability in more complex configurations.

#### 5.4. Side-heated natural convection in rectangular cavities with differing aspect ratios

Natural convection driven by differentially heated vertical walls in an enclosed cavity is one of the most common benchmark problems in prior RANS studies. Unlike the earlier cases in §5.1–5.3, where buoyancy production dominates the turbulence dynamics, the side-heated cavity is buoyancy-driven but not dominated by buoyancy production. Its long use as a validation case, combined with its distinct physical character, makes it a useful additional test for evaluating the robustness of the proposed correction.

The model performance is examined against the benchmark DNS datasets of Trias *et al.* (2007, 2010) and Sebilleau *et al.* (2018). The computational domain is two-dimensional, defined by  $0 \leq x \leq L$  and  $0 \leq z \leq H$ , with gravity acting in the  $-z$  direction. Two aspect ratios,  $H/L = 1$  and  $H/L = 4$ , are considered. The vertical walls are isothermal, with  $T = 0$  at  $x = 0$  and  $T = \Delta$  at  $x = L$ , while the horizontal walls are adiabatic. All boundaries satisfy the no-slip condition. The Prandtl number is fixed at  $Pr = 0.71$ , and the height-based Rayleigh number,  $Ra_H = g\beta\Delta H^3/(\nu\alpha)$ , is varied to characterise the resulting heat transfer.

For each pair of  $(Ra_H, H/L)$ , simulations are carried out on two grid resolutions and with both the corrected and uncorrected model formulations. The meshes use identical geometric growth in both directions and are constructed symmetrically about the mid-plane. When expressed in the normalised coordinates  $x/L$  and  $z/H$ , the same grid resolutions as in Section 5.3 are employed — Grid B ( $100^2$ ) and Grid C ( $150^2$ ).

Figure 16 presents the overall Nusselt number, defined as  $Nu = qL/(\alpha\Delta)$ , where  $q$  is the average heat flux through the vertical wall, as a function of  $Ra_H$  for the two aspect ratios. Across all four simulation cases, the differences in the predicted Nusselt numbers remain below 1.8%, and the mean discrepancy is less than 0.5%. These results indicate

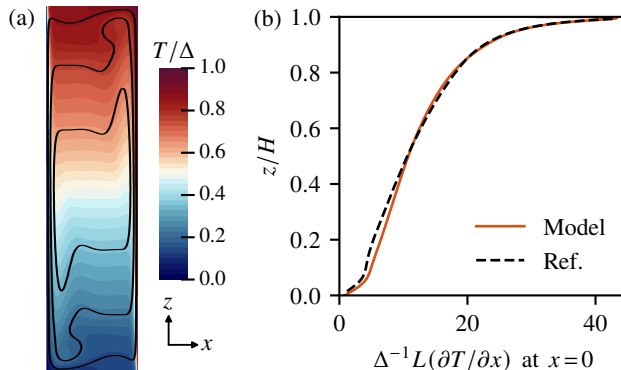


Figure 17. Simulation results of vertically heated natural convection for  $H/L = 4$  and  $Ra_H = 6.4 \times 10^8$ : (a) temperature field with streamfunction contours (black solid lines); (b) local heat-flux distribution along the cold wall (solid line). The dashed line denotes the DNS results of Trias *et al.* (2007).

that the solutions are effectively grid-independent and that the buoyancy correction yields a negligible change.

The weak influence of the buoyancy correction follows from the characteristics of this configuration. Most of the turbulent heat transport occurs horizontally while gravity acts vertically, so the magnitude of the buoyancy-production term remains small. In addition, the upper region of the cavity is warm and the lower region is cold, resulting in downward motion of cooled fluid and upward motion of heated fluid, which yields a negative buoyancy-production term. For all cases considered, the integrated negative contribution remains below roughly 5% of the shear production of  $k$ , indicating that buoyancy plays only a minor role in the modelled turbulence. This behaviour is consistent with the results reported by Peng & Davidson (1999), who examined the same side-heated cavity configuration and reported that predictions using the low-Reynolds-number  $k-\omega$  model of Wilcox (1994) are largely insensitive to the buoyancy coefficient  $C_{\omega b}$  for  $1 \leq H/L \leq 5$  and  $10^{10} \leq Ra_H \leq 10^{12}$ .

Further detail is shown in figure 17 for the case  $H/L = 4$  and  $Ra_H = 6.4 \times 10^8$ . Figure 17(a) shows the temperature field and streamfunction contours predicted by the model, which reproduce the expected features of side-heated natural convection, including thin thermal boundary layers along the isothermal vertical walls and corner-induced recirculation cells. Figure 17(b) presents the corresponding local heat flux distribution along the cold wall. The corrected and uncorrected models produce nearly identical profiles, and the mean flux corresponds to an overall Nusselt number of 16.3. Comparison with the DNS data of Trias *et al.* (2007) shows that the standard  $k-\omega$  model reproduces the heat-transfer distribution with high accuracy.

In summary, the side-heated cavity provides a useful check that the proposed buoyancy correction does not degrade the performance of the standard model in a shear-dominated regime. For this configuration, the standard  $k-\omega$  closure already reproduces the global Nusselt number and the local heat flux distribution with high accuracy, and the corrected and uncorrected formulations yield virtually identical results on two grid resolutions. Combined with the buoyancy-dominated cases examined in §5.1–5.3, these observations indicate that the proposed correction enhances the model response when buoyancy production is significant, while having negligible influence in configurations where buoyancy plays only a limited role.

## 6. Conclusions

This study establishes an analytically grounded framework for representing buoyancy effects in the standard  $k-\omega$  model, addressing the long-standing absence of a unified and physically motivated guideline for incorporating buoyancy in two-equation closures.

To that end, an explicit analytical solution of the standard formulation in one-dimensional Rayleigh–Bénard convection is derived. This solution reveals how the conventional buoyancy modelling determines the heat-transport scaling in natural convection and clarifies the origin of the model’s deviations from established  $Nu$ – $Ra$ – $Pr$  trends. Guided by this analysis, the closed-form correction functions emerge naturally rather than from empirical tuning, allowing the model to recover the observed scaling behaviour. Only two algebraic, dimensionless functions are introduced, and the formulation reduces to the original model in the absence of buoyancy, ensuring seamless compatibility and negligible computational overhead. The associated modelling coefficients are calibrated through a transparent and reproducible process using literature DNS and experimental datasets.

The revised model is evaluated across a wide range of buoyancy-driven configurations—including Rayleigh–Bénard convection in one- and two-dimensional settings, two internally heated convection systems, unstably stratified Couette flow, and vertically heated natural convection with varying aspect ratios. Across all cases, the corrected formulation substantially improves quantitative accuracy relative to the baseline model while maintaining robustness and numerical stability.

In summary, the proposed framework provides a systematic treatment of buoyancy effects within two-equation RANS closures and yields consistently accurate predictions of turbulent heat transport across a broad range of buoyancy-driven configurations and parameter regimes. Despite these strengths, several limitations remain outside the present scope. Because the model retains the gradient-diffusion hypothesis of the standard formulation, modest discrepancies in the temperature distribution may arise when the turbulent heat flux is not closely aligned with the mean temperature gradient. The calibration dataset could also be expanded; in particular, the low-Prandtl-number correction is limited by the scarcity of high- $Ra$  reference data for  $Pr < 1$ . Finally, other physical effects that can alter natural-convection dynamics, such as system rotation, are not considered here. These limitations suggest avenues for further refinement and for extending the present formulation to more complex buoyancy-affected flows.

**Funding.** This research received no specific grant from any funding agency, commercial or not-for-profit sectors.

**Declaration of interests.** The authors report no conflict of interest.

**Author ORCID.** D.-S. Joo, <https://orcid.org/0000-0002-2788-0648>

## REFERENCES

AHLERS, G., GROSSMANN, S. & LOHSE, D. 2009 Heat transfer and large scale dynamics in turbulent Rayleigh–Bénard convection. *Rev. Mod. Phys.* **81** (2), 503.

ANSYS, Inc. 2021a *Ansys CFX-Solver Theory Guide*, Release 2021 R2 edn.

ANSYS, Inc. 2021b *Ansys Fluent Theory Guide*, Release 2021 R2 edn.

ARFKEN, G.B., WEBER, H.J. & HARRIS, F.E. 2013 *Mathematical methods for physicists: a comprehensive guide*, 7th edn. Academic Press.

BLASS, A., TABAK, P., VERZICCO, R., STEVENS, R.J.A.M. & LOHSE, D. 2021 The effect of Prandtl number on turbulent sheared thermal convection. *J. Fluid Mech.* **910**, A37.

BLASS, A., ZHU, X., VERZICCO, R., LOHSE, D. & STEVENS, R.J.A.M. 2020 Flow organization and heat transfer in turbulent wall sheared thermal convection. *J. Fluid Mech.* **897**, A22.

BURCHARD, H. 2007 *Applied turbulence modelling in marine waters, Lecture Notes in Earth Sciences*, vol. 100. Springer.

BURCHARD, H. & BAUMERT, H. 1995 On the performance of a mixed-layer model based on the  $k-\varepsilon$  turbulence closure. *J. Geophys. Res. Oceans* **100** (C5), 8523–8540.

CHOI, S. K. & KIM, S. O. 2012 Turbulence modeling of natural convection in enclosures: A review. *J. Mech. Sci. Technol.* **26** (1), 283–297.

CRAFT, T. J., INCE, N. Z. & LAUNDER, B. E. 1996 Recent developments in second-moment closure for buoyancy-affected flows. *Dynam. Atoms. Oceans* **23** (1–4), 99–114.

DEHOUX, F., BENHAMADOUCHE, S. & MANCEAU, R. 2017 An elliptic blending differential flux model for natural, mixed and forced convection. *Int. J. Heat Fluid Flow* **63**, 190–204.

DOL, H. S. & HANJALIĆ, K. 2001 Computational study of turbulent natural convection in a side-heated near-cubic enclosure at a high Rayleigh number. *Int. J. Heat Mass Transf.* **44** (12), 2323–2344.

DOL, H. S., HANJALIĆ, K. & VERSTEEGH, T. A. M. 1999 A DNS-based thermal second-moment closure for buoyant convection at vertical walls. *J. Fluid Mech.* **391**, 211–247.

DURBIN, P. A. 2018 Some recent developments in turbulence closure modeling. *Ann. Rev. Fluid Mech.* **50** (1), 77–103.

DURBIN, P. A. & PETTERSSON-REIF, B. A. 2011 *Statistical Theory and Modeling for Turbulent Flows*, 2nd edn. John Wiley & Sons Ltd.

GARCIA-VILLALBA, M. & DEL ÁLAMO, J.C. 2011 Turbulence modification by stable stratification in channel flow. *Phys. Fluids* **23** (4).

GIBSON, M. M. & LAUNDER, B. E. 1978 Ground effects on pressure fluctuations in the atmospheric boundary layer. *J. Fluid Mech.* **86** (3), 491–511.

GOLUSKIN, D. & VAN DER POEL, E. P. 2016 Penetrative internally heated convection in two and three dimensions. *J. Fluid Mech.* **791**.

GOMEZ, S., GRAVES, B. & POROSEVA, S. 2014 On the accuracy of RANS simulations of 2D boundary layers with OpenFOAM. In *44th AIAA Fluid Dynamics Conference*, p. 2087.

GOMMERS, R. *et al.* 2025 Scipy 1.16.2. <https://doi.org/10.5281/zenodo.17101542>.

GROSSMANN, S. & LOHSE, D. 2000 Scaling in thermal convection: a unifying theory. *J. Fluid Mech.* **407**, 27–56.

HANJALIĆ, K. 2002 One-point closure models for buoyancy-driven turbulent flows. *Annu. Rev. Fluid Mech.* **34** (1), 321–347.

HANJALIĆ, K. & LAUNDER, B. 2011 *Modelling turbulence in engineering and the environment: second-moment routes to closure*. Cambridge university press.

HANJALIĆ, K. & LAUNDER, B. E. 2021 Reassessment of modeling turbulence via Reynolds averaging: A review of second-moment transport strategy. *Phys. Fluids* **33** (9).

HANJALIĆ, K. & VASIĆ, S. 1993 Computation of turbulent natural convection in rectangular enclosures with an algebraic flux model. *Int. J. Heat Mass Transf.* **36** (14), 3603–3624.

HENKES, R. A. W. M., VLUKT, F. F. VAN DER & HOOGENDOORN, C. J. 1991 Natural-convection flow in a square cavity calculated with low-Reynolds-number turbulence models. *Int. J. Heat Mass Transfer* **34** (2), 377–388.

INCE, N. Z. & LAUNDER, B. E. 1989 On the computation of buoyancy-driven turbulent flows in rectangular enclosures. *Int. J. Heat Fluid Flow* **10** (2), 110–117.

JOO, D.-S. 2025 A global similarity correction for Reynolds-averaged Navier–Stokes modeling of unstable stratification in natural convection flows. *Phys. Fluids* **37** (7).

JOO, D.-S. & YOU, D. 2024 A Reynolds-averaged Navier–Stokes closure for steady-state simulations of Rayleigh–Bénard convection. *Phys. Fluids* **36** (8).

KENJEREŠ, S., GUNARJO, S. B. & HANJALIĆ, K. 2005 Contribution to elliptic relaxation modelling of turbulent natural and mixed convection. *Int. J. Heat Fluid Flow* **26** (4), 569–586.

KENJEREŠ, S. & HANJALIĆ, K. 1995 Prediction of turbulent thermal convection in concentric and eccentric horizontal annuli. *Int. J. Heat Fluid Flow* **16** (5), 429–439.

KULACKI, F. A. & EMARA, A. A. 1977 Steady and transient thermal convection in a fluid layer with uniform volumetric energy sources. *J. Fluid Mech.* **83** (2), 375–395.

LAUNDER, B. E. & SHARMA, B. I. 1974 Application of the energy-dissipation model of turbulence to the calculation of flow near a spinning disc. *Lett. Heat Mass Transf.* **1** (2), 131–137.

LAUNDER, B. E. 2005 RANS modelling of turbulent flows affected by buoyancy or stratification. *Predict. Turbul. Flows* pp. 50–127.

LAZEROMS, W. M. J., BRETHOUWER, G., WALLIN, S. & JOHANSSON, A. V. 2013 An explicit algebraic Reynolds-stress and scalar-flux model for stably stratified flows. *J. Fluid Mech.* **723**, 91–125.

LI, X.-M., HE, J.-D., TIAN, Y., HAO, P. & HUANG, S.-D. 2021 Effects of Prandtl number in quasi-two-dimensional Rayleigh–Bénard convection. *J. Fluid Mech.* **915**, A60.

MARKATOS, N. C. & PERICLEOUS, K. A. 1984 Laminar and turbulent natural convection in an enclosed cavity. *Int. J. Heat Mass Transf.* **27** (5), 755–772.

NASA Langley Research Center 2024 Wilcox  $k-\omega$  model — turbulence modeling resource. <https://turbmodels.larc.nasa.gov>, last updated 4 October 2024.

NIEMELÄ, J. J., SKRBEK, L., SREENIVASAN, K. R. & DONNELLY, R. J. 2000 Turbulent convection at very high Rayleigh numbers. *Nature* **404** (6780), 837–840.

NOURGALIEV, R. R. & DINH, T. N. 1997 The investigation of turbulence characteristics in an internally-heated unstably-stratified fluid layer. *Nucl. Eng. Des.* **178** (3), 235–258.

OPENCFD LTD. 2025 OpenFOAM: The Open Source CFD Toolbox, API Guide, v2412. <https://www.openfoam.com>.

PANDEY, A., KRASNOV, D., SREENIVASAN, K. R. & SCHUMACHER, J. 2022 Convective mesoscale turbulence at very low Prandtl numbers. *J. Fluid Mech.* **948**, A23.

PENG, S.-H. & DAVIDSON, L. 1999 Computation of turbulent buoyant flows in enclosures with low-Reynolds-number  $k-\omega$  models. *Int. J. Heat Fluid Flow* **20** (2), 172–184.

PETTERSSON REIF, B. A., GATSKI, T. B. & RUMSEY, C. L. 2006 On the behavior of two-equation models in nonequilibrium homogeneous turbulence. *Phys. Fluids* **18** (6).

POPE, S. B. 2000 *Turbulent Flows*. Cambridge University Press.

RODI, W. 1980 *Turbulence Model and Their Application in Hydraulics: A state of the Art Review*. Int. Ass. for Hydraulic Research, Delft, The Netherlands.

RODI, W. 1987 Examples of calculation methods for flow and mixing in stratified fluids. *J. Geophys. Res. Oceans* **92** (C5), 5305–5328.

RUMSEY, C. L. 2007 Apparent transition behavior of widely-used turbulence models. *Int. J. Heat Fluid Flow* **28** (6), 1460–1471.

RUMSEY, C. L., PETTERSSON REIF, B. A. & GATSKI, T. B. 2006 Arbitrary steady-state solutions with the  $k-\varepsilon$  model. *AIAA J.* **44** (7), 1586–1592.

SEBILLEAU, F., ISSA, R., LARDEAU, S. & WALKER, S. P. 2018 Direct numerical simulation of an air-filled differentially heated square cavity with Rayleigh numbers up to  $10^{11}$ . *Int. J. Heat Mass Transf.* **123**, 297–319.

STEVENS, R. J. A. M., LOHSE, D. & VERZICCO, R. 2011 Prandtl and Rayleigh number dependence of heat transport in high Rayleigh number thermal convection. *J. Fluid Mech.* **688**, 31–43.

STORN, R. & PRICE, K. 1997 Differential evolution—a simple and efficient heuristic for global optimization over continuous spaces. *J. Glob. Optim.* **11** (4), 341–359.

TOGNI, R., CIMARELLI, A. & ANGELIS, E. DE 2015 Physical and scale-by-scale analysis of Rayleigh–Bénard convection. *J. Fluid Mech.* **782**, 380–404.

TRIAS, F. X., GOROBETS, A., SORIA, M. & OLIVA, A. 2010 Direct numerical simulation of a differentially heated cavity of aspect ratio 4 with Rayleigh numbers up to  $10^{11}$ —part I: Numerical methods and time-averaged flow. *Int. J. Heat Mass Transf.* **53** (4), 665–673.

TRIAS, F. X., SORIA, M., OLIVA, A. & PÉREZ-SEGARRA, C. D. 2007 Direct numerical simulations of two- and three-dimensional turbulent natural convection flows in a differentially heated cavity of aspect ratio 4. *J. Fluid Mech.* **586**, 259–293.

VERZICCO, R. & CAMUSSI, R. 1999 Prandtl number effects in convective turbulence. *J. Fluid Mech.* **383**, 55–73.

VIOLET, P. L. 1987 The modelling of turbulent recirculating flows for the purpose of reactor thermal-hydraulic analysis. *Nucl. Eng. Des.* **99**, 365–377.

WILCOX, D. C. 1994 Simulation of transition with a two-equation turbulence model. *AIAA journal* **32** (2), 247–255.

WILCOX, D. C. 2006 *Turbulence Modeling for CFD*, 3rd edn. DCW industries, Inc. La Canada.

WÖRNER, M., SCHMIDT, M. & GRÖTZBACH, G. 1997 Direct numerical simulation of turbulence in an internally heated convective fluid layer and implications for statistical modelling. *J. Hydraul. Res.* **35** (6), 773–797.

XIA, K.-Q., LAM, S. & ZHOU, S.-Q. 2002 Heat-flux measurement in high-Prandtl-number turbulent Rayleigh–Bénard convection. *Phys. Rev. Lett.* **88** (6), 064501.

YERRAGOLAM, G. S., STEVENS, R. J. A. M., VERZICCO, R., LOHSE, D. & SHISHKINA, O. 2022 Passive scalar transport in couette flow. *J. Fluid Mech.* **943**, A17.